

MASARYKOVA UNIVERZITA
PŘÍRODOVĚDECKÁ FAKULTA
ÚSTAV TEORETICKÉ FYZIKY A ASTROFYZIKY

Bakalářská práce

BRNO 2022

KATEŘINA PIVOŇKOVÁ

**MASARYKOVA
UNIVERZITA**
PŘÍRODOVĚDECKÁ FAKULTA
ÚSTAV TEORETICKÉ FYZIKY A ASTROFYZIKY

Spectral variability of evolved supergiants: study of HD 21389

Bakalářská práce

Kateřina Pivoňková

Vedoucí práce: Olga Viktorovna Maryeva, Ph.D.

Brno 2022

Bibliografický záznam

Autor:	Kateřina Pivoňková Přirodovědecká fakulta, Masarykova univerzita Ústav teoretické fyziky a astrofyziky
Název práce:	Název práce
Studijní program:	PřF B-FY Fyzika
Studijní obor:	PřF ASTRO Astrofyzika
Vedoucí práce:	Olga Viktorovna Maryeva, Ph.D.
Akademický rok:	2021/2022
Počet stran:	xiii + 68
Klíčová slova:	HD 21389; veleobr spektrálního typu A; spektroskopie; proměnnost typu α Cyg; radialní rychlosti, čára H α

Bibliographic Entry

Author: Kateřina Pivoňková
Faculty of Science, Masaryk University
Department of theoretical physics and astrophysics

Title of Thesis: Spectral variability of evolved supergiants: study of HD 21389

Degree Programme: PřF B-FY Physics

Field of Study: PřF ASTRO Astrophysics

Supervisor: Olga Viktorovna Maryeva, Ph.D.

Academic Year: 2021/2022

Number of Pages: xiii + 68

Keywords: HD 21389; A-type supergiant; spectroscopy; α Cyg type variability, radial velocities; H α line

Abstrakt

HD 21389 je veleobr spektrální třídy A, který patří mezi proměnné hvězdy typu α Cyg. Přestože je hvězda HD 21389 již více než sto let pozorována, stále se o ní z jejích spekter dozvídáme nové poznatky. Cílem této práce je shrnout informace o této hvězdě a doplnit je o výsledky analýzy spekter, pořízených mezi lety 2017 až 2022, ve viditelné oblasti Perkovým 2m dalekohledem a 1.5m dalekohledem AZT-12 v Estonsku.

Abstract

HD 21389 is an A-type supergiant star that belongs to α Cyg variables. However, this star undergoing continuous observation for more than one hundred years still reveals new findings. This thesis aims to summarize information about this star and expand them for our results based on the analysis of spectra taken from 2017 up to 2022 in the optical region by Perek 2-m and AZT-12 telescopes.

ZADÁNÍ
BAKALÁŘSKÉ PRÁCE

Akademický rok: 2021/2022

Ústav:	Ústav teoretické fyziky a astrofyziky
Studentka:	Kateřina Pivoňková
Program:	Fyzika
Specializace:	Astrofyzika

Ředitel *ústavu* PŘF MU Vám ve smyslu Studijního a zkušebního řádu MU určuje bakalářskou práci s názvem:

Název práce:	Spectral variability of evolved supergiants: study of HD 21389
Název práce anglicky:	Spectral variability of evolved supergiants: study of HD 21389
Jazyk závěrečné práce:	angličtina

Oficiální zadání:

Studies of spectral variability of B-A supergiants are important for both theory of stellar evolution as well as theory of physical process in stellar atmospheres (clumping, pulsations, magnetic fields). HD21389 star that belongs to Camelopardalis OB1 stellar association is a good target for getting a hands-on experience in modern astronomical spectroscopy, from both observational and theoretical points of view. The star displays a strong spectral variability – the hydrogen Ha line in its spectrum changes profile from absorption to broad emission on a time scale of a few months. Studying it will allow the student to get the following skills: 1) participation in observations on Perek's 2-m telescope at the Ondřejov observatory of ASU CAS; 2) data reduction of long-slit and echelle spectra obtained at Perek's 2-m telescope at the Ondřejov observatory of ASU CAS; 3) working with modern software packages for spectral analysis; 4) understanding the modern theory of stellar evolution. Expected result: a detailed description of the spectral variability and determination of the star's evolutionary status

Vedoucí práce:	Olga Viktorovna Maryeva, Ph.D.
Datum zadání práce:	2. 11. 2021
V Brně dne:	23. 5. 2022

Zadání bylo schváleno prostřednictvím IS MU.

Kateřina Pivoňková, 14. 1. 2022

Olga Viktorovna Maryeva, Ph.D., 15. 1. 2022

RNDr. Luboš Poláček, 19. 1. 2022

Poděkování

Na prvním místě bych ráda poděkovala vedoucí mé práce Olze Victorievně Maryevě, Ph.D. za její podporu, rady a náměty, trpělivost, za všechny příležitosti, které mi poskytla. A zejména čas, který mně a této práci věnovala.

Dále pozorovatelům z Tartu Observatory v Estonsku a pozorovatelům ze Stelárního oddělení Astronomického ústavu Akademie věd České Republiky v Ondřejově za pořízení spekter a zaškolení do jejich zpracování. Také bych ráda poděkovala Anně Aret, PhD, Michaele Kraus, PhD a doc. RNDr. Jiřímu Kubátovi, CSc. za diskuse a cenné rady.

Velkou oporou mi byla po celou dobu i má rodina a přátelé.

Prohlášení

Prohlašuji, že jsem svoji bakalářskou práci vypracovala samostatně pod vedením vedoucího práce s využitím informačních zdrojů, které jsou v práci citovány.

Brno 23. května 2022

.....
Kateřina Pivoňková

Contents

Introduction	1
1. HD 21389 as One of the Deneb Type Variables	3
1.1 Massive Stars and Deneb Type Variables	3
1.2 Biography of HD 21389	5
2. Observations and Spectral Data Reduction	11
2.1 Telescopes and Instruments	11
2.2 Data Reduction	13
2.2.1 Data Reduction in IRAF	13
2.3 Additional Procedures	18
2.3.1 Telluric Correction	18
2.3.2 Velocity Correction	19
2.3.3 Normalization	20
2.3.4 Reduction of OES Spectra	20
3. Spectral Variability Analysis	23
3.1 DIB Lines Correction	24
3.2 Telluric Correction	25
3.3 Spectrum of HD 21389	26
3.4 Variability in H α line	26
3.4.1 Broad Emission Wings around Balmer Lines	29
3.5 Sign of Binary Character	32
3.6 Variability in Other Spectral Lines	32
3.6.1 Data from D700	33
3.6.2 Data from ASP-32	35
3.6.3 OES Data	36
3.6.4 Short time changes	40
Conclusion	47
Bibliography	49
Appendix	55

Introduction

Based on strength of absorption lines the stars were systematically divided into 7 classes named by letters (O, B, A, F, G, K, M). Later it turned out that this was not enough and therefore each sequence has been subdivided by numbers (O2, O3 . . . , O9, B0, . . .) where the hottest stars belong to 0 and cooler to 9 - excluding the O sequence which starts by O2. They are often designated as early (hotter) or late (cooler) type stars. Moreover, the stars are assigned with the luminosity class (Ia⁺, Ia, Iab, Ib, II, III, . . . , VII).

B- to A-type supergiants (Ia) are massive stars bright enough to be easily observed even at a large distance. The complex physics of their atmospheres makes them interesting objects for further study not only in this field but also for stellar evolution in the upper part of the H–R diagram, asteroseismology, and galactic physics with regard to the study of the ionized H II regions.

Late B- and early A-type supergiants are known for decades to show variability in brightness and radial velocities. However, this group of stars undergoing continuous observation, the mechanism responsible for such changes is not well understood. In a way to better understand and describe the mechanism a detailed and continuous study of an early type supergiants is required.

This study presents results based on five years of spectroscopic observation of A-type supergiant HD 21389. Optical spectra mainly in the H α region were taken by Perek's 2-meter telescope at the Astronomical Institute of Czech Academy of Science and AZT-12 1.5-meter telescope at the Tartu Observatory which belongs to the University of the Tartu in Estonia.

HD 21389 has been observed for the first time to show variability more than one century ago. Since that time undergoing continuous spectroscopic observation and still reveal new findings on the variability of supergiants. This star is a member of α Cyg variables which main characteristics are described in the first chapter together with its physical characteristics and overview of past observations.

First chapter is then followed by the description of spectral data proceeding and it is supplemented by information about the instruments used for data collection.

In the third chapter, which is the last one, the spectral data analysis is discussed. H α line as the most extensively studied spectral line shows the complex structure, which is typical for supergiant stars. Although this star has been observed many times in the past, no one ever mentions the presence of an extended emission feature around Balmer lines, which is most prominent around H α . Moreover, this study discusses observed variability in the strength of this emission feature. Lines' profile variability and variability in radial velocities of selected lines are analyzed with a possible sign of binary character.

We believe that our results may be useful for further studies of these rare stars.

Chapter 1

HD 21389 as One of the Deneb Type Variables

1.1 Massive Stars and Deneb Type Variables

Massive stars are stars with initial masses between $8M_{\odot}$ and $150M_{\odot}$ that are spread in the upper part of the Hertzsprung–Russell (H–R) diagram. Such stars form a degenerate iron core that eventually leads to an explosion of a core-collapse supernova (SN), a long-lasting gamma-ray burst (GRB), or a direct collapse into a black hole. Massive stars in comparison to Sun-like stars have a much shorter lifetime ranging from units to several tens of Myr, which made them quite rare. Their fast passage through H–R diagram, from Main Sequence to Red Supergiants (RSGs) or Wolf–Rayet stars (WR) depending on initial mass. During their evolution may cross stages Blue supergiants (BSG), Luminous Blue Variables (LBVs), and even the Yellow Hypergiants (YHGs) phase. After leaving Main Sequence they starting show variability where some of them manifest themselves as α Cygni type variables.

Deneb Type Variables

α Cygni (α Cyg), also known as Deneb, is a high luminous star of A2 Ia spectral type. It exhibits low amplitude photometric variability ($\Delta V \leq 0.1$ mag) and variability in radial velocity with period 1.2 - 100 day (Catelan and Smith 2015). Its position in the night sky makes Deneb (in the northern hemisphere it may be observed for almost a whole year) one of the most studied A-type supergiants. With its specific type of variability, Deneb became the prototype of a group of stars showing similar behavior known as α Cyg variables.

For this class of objects, the variability in line profiles is typical, especially $H\alpha$ (λ 6563) shows changes in the shape of the profile and its strength. The behavior of $H\alpha$ can be attributed to the star's rotation variability with additional stellar wind modulation (Kaufer, Stahl, Wolf, Gaeng, Gummersbach, Kovacs, et al. 1996). Photospheric lines reveal a special pattern of spectral variability too pointing to cyclic variations in radial velocities, which are still thought to be caused by stellar oscillations. This possibly indicates simultaneous excitation of pulsation modes typical by period for non-radial oscillations and radial overtones (Achmad, Lamers, and Pasquini 1997). Simultaneous spectroscopic (Lucy

1976) and photometric observation (Fath 1935) point to a correlation between changes in the brightness and variability in radial velocities of Deneb.

The variability of those stars is significantly stronger on timescale and in amplitudes toward the lower temperatures, which is why it is easier to observe these processes in A-type supergiants (Lefever, Puls, and Aerts 2007). However long time scales and low amplitudes indicating these variables are responsible for further work which needs to be done to characterize the nature of the variability of this class. Today's knowledge about the mechanism underlying the variability of such stars is still not well understood.

As an explanation of variability observed in Deneb the non-radial oscillations are essential. The study of Deneb was advanced by Lucy 1976 where the multiple modes oscillations are discussed in connection to low-frequency gravity modes (g-modes) pulsations. H. Saio et al. 2006 found g-mode pulsations trapped in a convective zone just above the H-burning shell as a possible source of long periodic oscillations in HD 163899. Although this star is now classified as Slowly Pulsating B-type Supergiant (SPBsg), it has been included in α Cyg variables. Also for α Cyg, the investigation by Gautschy 2009 gives the evidence of sub-photospheric convective zone (found in massive stars in the post-main sequence phase) causing the variability.

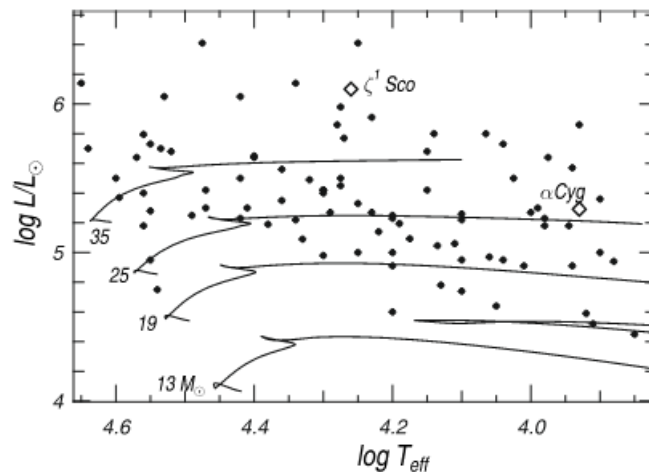


Figure 1.1: H–R diagram showing position of sample of α Cyg variables and SPBsg. Taken from Gautschy 2009.

Moreover, the occasional appearance of deep and highly blue-shifted absorptions, known as high-velocity absorption events (HVAs), was detected for a few α Cyg variables. The kinematic properties of the HVAs are completely different from those of Discrete Absorption Components (DACs) observed in the ultraviolet spectra of O-type and early B-type mass-losing stars. Similar scenario consisting of large-scale wind structure grounded in the photosphere was suggested to clarify their appearance and development (Markova et al. 2008). α Cyg variables with HVA events are rare, and occasions of HVAs' appearance are just a little studied.

The positions of α Cyg variables in the H–R diagram (Fig. 1.1) is consistent with pre- and post-red supergiant phase (Hideyuki Saio, Cyril Georgy, and Georges Meynet 2013). However, their observable pulsation modes may be the evidence that the star already passed

through the red supergiant stage during which lost a significant amount of mass due to the strong stellar wind.

1.2 Biography of HD 21389

HD 21389 is an evolved supergiant star located in the Camelopardalis constellation. Its stellar parameters are listed in Tab. 1.2. Now it is included in a list of Galactic α Cyg variables (e.g. Straižys and Laugalys 2007) and it is not that long since HD 21389 was assigned as a member of the OB1 association in Camelopardalis (Lyder 2001).

OB1 Association in Camelopardalis

Association Cam OB1 was identified for the first time by Morgan, Whitford, and Code 1953. The size of the OB1 Cam association seems to be scattered into 12° in latitude and about 24° in longitude. The study by Straižys and Laugalys 2007 revealed that the association consists of three independent subgroups Group A, Group B, and Group C formed by the open cluster NGC 1502. HD 21389 belongs to Group A, where illuminates the reflection nebulae vdB15. Except for this one Group A contains another nebulae vdB14 and ionized region of H II Sh 2-202. In study by Straižys and Laugalys 2008 the distance of association was estimated. By taking the average distance of 26 selected M and K type stars the result gives an average distance of 1010 ± 210 pc, which is very close to the value estimated based on *Gaia* data for HD 21389 (Tab. 1.2).

History of Observation and Stellar Parameters of HD 21389

Spectroscopic study of HD 21389 began in 1911 when Mr. Young found variability in its radial velocity. The star was suggested as a spectroscopic binary (Campbell et al. 1911).

Later, in study by Abt 1957 the radial velocities of Si II (λ 4028, 4030) and Fe II (λ 4508, 4515, 4520, 4522) lines were measured. Radial velocity curves obtained from these lines have a very similar shape and are shifted relative to each other. It was considered that during the elapsed observation there is one more maximum at 15.4 day-long interval, then the period is about 7.7 days. Moreover, the study by Percy and Welch 1983 revealed the period of photometric variability of this star between 6 to 15 days which is close to what was derived from spectroscopic data by Abt 1957.

A few A-type supergiants were subjected to a study by Aydin 1972. Based on the results of observed changes for all investigated supergiants the pulsations of a complex character were suggested. In the case of HD 21389 the investigation of radial velocities of Balmer lines revealed the contraction phase of its atmosphere. Also, variability in metallic lines was found. Afterward, this has been confirmed by many other studies (e.g. Denizman and Hack 1988; Maharramov and Baloglanov 2015; Zeinalov and Rzaev 1990a). The atmosphere of HD 21389 is suspected to be in the contraction phase at some epoch and expansion phase at another epoch.

Parameters	Values	References
Names	HR 1040, CE Cam, BD+58 607	[3] accessed September 20, 2021
Observed Parameters		
RA J2000	$3^h 29^m 54.7^s$	Gaia Collaboration 2020
DEC J2000	$58^\circ 52' 43.5''$	Gaia Collaboration 2020
M_V [mag]	-7.56	
V [mag]	4.54	Ducati 2002
B [mag]	5.10	Ducati 2002
Spectral Type	A0 Ia	Lyder 2001
Parallax [mas]	0.930 ± 0.119	Gaia Collaboration 2020
Estimated Parameters		
T_{eff} [K]	9730	Verdugo, Talavera, and Gómez de Castro 1999b
M [M_\odot]	19.3	Verdugo, Talavera, and Gómez de Castro 1999b
R [R_\odot]	97	Verdugo, Talavera, and Gómez de Castro 1999b
$\log L/L_\odot$	4.87	de Jager, Nieuwenhuijzen, and van der Hucht 1988
$\log g$ [cgs]	1.7	Takeda and Takada-Hidai 2000
v_{esc} [$\text{km} \cdot \text{s}^{-1}$]	233	Talavera and Gomez de Castro 1987
$v \cdot \sin i$ [$\text{km} \cdot \text{s}^{-1}$]	53	Verdugo, Talavera, and Gómez de Castro 1999b
\dot{M} [$M_\odot \cdot \text{yr}^{-1}$]	$-4.2 \cdot 10^{-7}$	Barlow and Cohen 1977
Distance [pc]	954^{+328}_{-196}	Bailer-Jones, Rybizki, Fouesneau, Mantelet, et al. 2018
Distance [pc]	1084^{+124}_{-112}	Bailer-Jones, Rybizki, Fouesneau, Demleitner, et al. 2021

Table 1.1: Stellar parameters for HD 21389.

Rosendhal [1973](#) studied mainly $H\alpha$ line in early-type stars and for HD 21389 noted double-peak emission and in connection to metallic line variability, has been observed asymmetry in lines' profile of He I ($\lambda 6678$).

Particularly interesting is the estimation of mass loss rate \dot{M} from free-free emission at $10 \mu\text{m}$ by Barlow and Cohen [1977](#), who used Eq. [1.1](#) derived by Wright and Barlow [1975](#). For HD 21389 the value of v_∞ was interpolated from values of 10 supergiants, already published by Snow and Morton [1976](#), which are typical velocities of the short-wavelength edges of the P Cyg absorption part of lines in the ultraviolet region.

$$\dot{M} = 0.095 \frac{\mu v_\infty S_\nu^{4/3} D^{3/2}}{Z \gamma^{1/2} g^{1/2} v^{1/2}}, \quad (1.1)$$

where S_ν is the free-free flux at frequency ν , D is distance in kpc (0.82 kpc), μ is the mean atomic gas weight, Z is the mean ionic charge of the gas, γ is the mean number of electrons per ion and $g(\nu, T)$ is the Gaunt factor. In this case $\mu = 1.26$, $Z = 1.0$, and $\gamma = 1.0$. Values of the Gaunt factor $g(\nu, T)$ were taken from Karzas and Latter [1961](#), where wind temperature was identified with effective temperature of the star. For HD 21389 the value of v_∞ was interpolated from values of 10 supergiants, already published by Snow and Morton

1976, which are typical velocities of the short-wavelength edges of the P Cyg absorption part of lines in the ultraviolet region. In 1978 the star has been first observed in the ultraviolet region by International Ultraviolet Explorer (IUE) space observatory (Praderie, Talavera, and Lamers 1980). The α Cyg was included among the observed objects. From line profile comparison (Mg II, Si II and C II) between HD 21389 and α Cyg the mass loss rate was estimated to the order of $10^{-8} M_{\odot} \cdot \text{yr}^{-1}$. The value of \dot{M} is consistent with results predicted by Kunasz, N. D. Morrison, and Spressart 1983. Based on computed profiles for Mg II ($\lambda 2802$) they published that $\dot{M} < 1.5 \cdot 10^{-10} M_{\odot} \cdot \text{yr}^{-1}$ is excluded because line became optically thin in the wind, on the other hand $\dot{M} > 8.5 \cdot 10^{-8} M_{\odot} \cdot \text{yr}^{-1}$ is possible, but not explored to be consistent with Mg II profile.

Based on observations taken from 1977 to 1987 Denizman and Hack 1988 noted two different profiles of $H\alpha$ line. Blue shifted absorption with highly variable profiles without any emission component, which were taken during one night. And double-peak emission with a central absorption component. Variability was recorded in radial velocities and mainly in lines' profile of $H\beta$, which shows double-peak absorption and from time to time is more or less symmetric. First spectra taken during one night present a possible expansion, although those which were obtained within one day point to a moderate contraction phase. Later it turned back to the expansion.

This star presents a complex structure of $H\alpha$ line profile. Zeinalov and Rzaev 1990a tried to systematically describe the evolution of the $H\alpha$ line profile over time. Based on about a dozen spectra they proposed two scenarios:

- (1) absorption profile turns to P Cyg and it changes to an inverse P Cyg profile, finally it goes back to pure absorption
- (2) absorption profile changes to an inverse P Cyg, it turns to a normal P Cyg and back to the absorption

Denizman and Hack 1988 studied spectra of three white supergiant stars including HD 21389. Observed asymmetric $H\alpha$ line profiles showed expansion phase and similar rapid variability was found in line profile and radial velocities of $H\beta$ which was also confirmed by Verdugo, Talavera, and Gómez de Castro 1999b. In addition for $H\beta$ line was reported to have faint emission wings Gray and Garrison 1987.

In 1999 Verdugo, Talavera, and Gómez de Castro 1999b estimated the mass M of HD 21389 using interpolation between evolutionary tracks by Schaller et al. 1992 for solar metallicity and assumption that A-type supergiants have evolved straight away from the main sequence. And radius was calculated from

$$M_{bol} = 42.31 - 5 \log \frac{R}{R_{\odot}} - 10 \log T_{\text{eff}}. \quad (1.2)$$

In way to find a fitting value of T_{eff} and $\log g$ the method laying in searching for convergence of infrared flux, equivalent widths of Balmer lines, Balmer discontinuity and ionization equilibrium in T_{eff} vs $\log g$ plane was applied. It was done in correspond to modeled spectra (generated by ATLAS 9) without account of highly structured envelope which is typical for A-type supergiants and also crucial because processes related to existence of circumstellar envelope are expected to be relevant.

Corliss, Nancy D. Morrison, and S. J. Adelman 2015 performed the most comprehensive study of spectral variability of HD 21389 for today. They analyzed 152 spectra obtained with a 1-m telescope of Ritter Observatory between 1993 and 2007. This study also presents results of photometric observation which was in some seasons simultaneously covered by spectroscopic observation. Photometric changes of HD 21389 are of course strongly tied to its active phases, thus the star in quiescent ones shows less variability.

Maharramov and Baloglanov 2015 investigated mainly the behavior of $H\alpha$ and $H\beta$ line. In addition for this star the radial velocities of Na I D ($\lambda 5890; 5896$) lines were measured. Both Balmer lines revealed changes in lines' profiles, whereas the profile of $H\alpha$ in active phases was associated with asymmetries in the profile of Na I D.

The value of absolute stellar magnitude M_V (in Tab. 1.2) was calculated from the distance modulus including extinction

$$M_V = m_V - 5 \log r + 5 - A_V, \quad (1.3)$$

where extinction $A_V = 3.1 \cdot E_{(B-V)} = 3.1 \cdot [(B-V) - (B-V)_0]$ and color index $(B-V)_0 = -0.06$ mag was taken from [here](#) corresponding to A0 type supergiants.

Evolutionary Phase and Location in Hertzsprung–Russell diagram

Characteristics	Pre-red supergiant stage	Post-red supergiant stage
Age (comparison with age estimated from cluster or association membership)	11.8 Myr time to reach the RSG stage (estimated from stellar evolutionary models according to its mass)	12.4 Myr time to leave the RSG stage (estimated from stellar evolutionary models according to its mass)
Abundance	comparable with solar abundances H=0.68 He=0.30 N= $3 \cdot 10^{-3}$ C= $1 \cdot 10^{-3}$ O= $4.6 \cdot 10^{-3}$	due to internal mixing and mass loss during the red supergiant stage their surface will be enriched by already processed C N O H=0.55 He=0.44 N= $4.7 \cdot 10^{-3}$ C= $5.2 \cdot 10^{-4}$ O= $3.4 \cdot 10^{-3}$
Pulsations (α Cyg variables)	almost no radial pulsations are excited	many radial and non-radial pulsations are excited

Table 1.2: Comparison of stellar characteristics in two stages – pre- and post-red supergiant stage. Age and abundances are taken from Geneva evolution track for star with $17M_{\odot}$. [4] accessed April 17, 2022

Association membership, pulsations, and chemical composition of the atmosphere can help us to better understand an actual evolutionary stage of a star. Depending on the type of this star it can be said that it is somewhere in the red supergiant evolutionary stage or close to (pre- or post-red supergiant evolutionary stage).

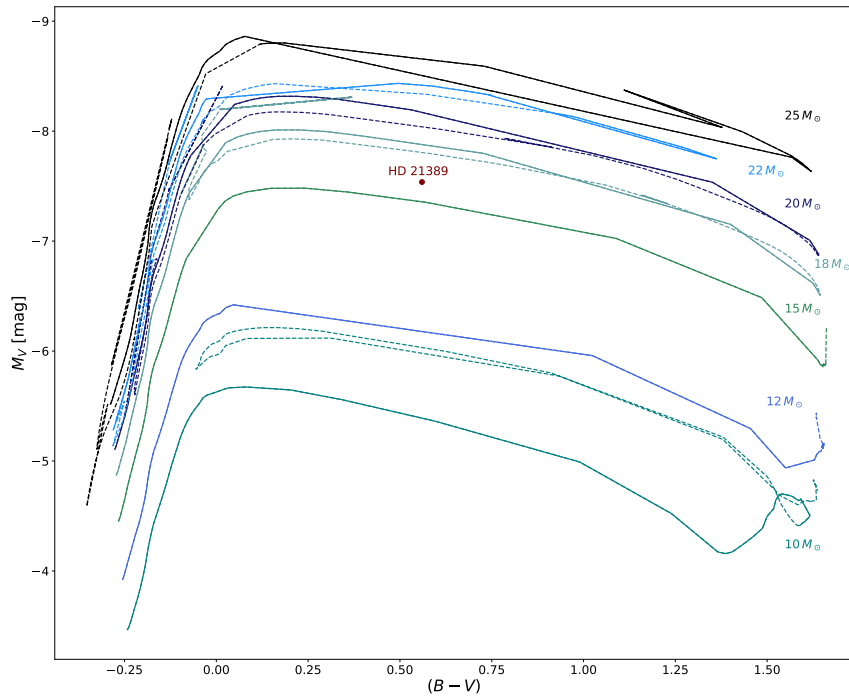


Figure 1.2: Modeled stellar evolutionary tracks of stars with initial masses of $10 M_{\odot}$, $12 M_{\odot}$, $15 M_{\odot}$, $18 M_{\odot}$, $20 M_{\odot}$, $22 M_{\odot}$ and $25 M_{\odot}$. The maroon dot represents the position of HD 21389 in H–R diagram. Tracks were computed with mass, metallicity ($Z = 0.014 = Z_{\odot}$) and rotation rate ($\Omega/\Omega_{crit} = 0.568$) as an input parameters. Data are available [here](#) and were published by Ekström et al. 2012.

During the persistence on the RSGs stage the changes in atmospheric abundances are expected. In the study by Corliss, Nancy D. Morrison, and S. J. Adelman 2015 the N/C and N/O ratios were estimated and compared with the the Sun. In comparison to α Cyg which is referred to be in the post-red supergiant stage by Przybilla et al. 2010 are the values for HD 21389 similar to the solar values which suggested that HD 21389 is in pre-red supergiant stage.

According to C. Georgy, H. Saio, and G. Meynet 2014 most Deneb type variables exhibit a few pulsation modes during their first crossing, while much more pulsation modes are excited during the second crossing of the H–R diagram.

To summarize, the evolutionary stage of HD 21389 according to its atmospheric abundances and pulsational characteristics this star has not undergone the internal mixing in the red supergiant stage, and its pulsations don't point to the presence of multiperiodic behavior. So HD 21389 is probably evolving right in its first crossing which is consistent with the position of the Deneb type variables in the H–R diagram.

Chapter 2

Observations and Spectral Data Reduction

2.1 Telescopes and Instruments

Spectra used for this thesis were obtained with Perek's 2-meter telescope of the Astronomical Institute of the Czech Academy of Sciences and the 1.5-meter telescope AZT-12 of Tartu University, Estonia. Both telescopes are seen in Fig. 2.1.

Refractor AZT-12 is a 1.5-meter telescope is located at Tartu Observatory in Tõravere. Its parameters make it the largest telescope in Northern Europe. The telescope was installed between 1974 and 1975. Since 1976 is still actively used for astronomical observations mostly by researchers of the Department of Stellar Physics at the Tartu Observatory.

Perek's 2-meter is the largest telescope in the Czech Republic. The telescope is operating since 1967 and it is still used for scientific observations mainly research in the Czech Republic. Since the telescope is in operation, passed through many upgrades. Going back to 2007 the driving electronics were replaced by the modern ones. In 2009 the mirrors were recoated. During 2019, due to decreasing efficiency of the optical system, the optical configuration was changed. After this improvement, the light travels from the primary focus through optical fibers. [1] [accessed September 20, 2021](#)

Observations of HD 21389 by Perek's 2-meter telescope were carried out with two spectrographs: Ondřejov Echelle Spectrograph (OES) (Kabáth et al. 2020; Koubsky et al. 2004), and Single order spectrograph (D700) (Slechta and Skoda 2002). For observations with AZT-12 in Tõravere longslit spectrograph ASP-32 was used.

Ondřejov Echelle Spectrograph (OES)

OES is a fibre-fed high-resolution spectrograph installed separately from the telescope in a room with a stable temperature. As it is mentioned above, the light goes from the primary focus through optical fibers to the coudé room. It is reflected there to an echelle grating. Then the optical mirror reflects the light further to an equilateral prism. After orders are separated go to the detector. Detector itself is nitrogen-cooled to a working temperature -110°C . One fibre is independently used for the flat field calibration lamp and Thorium-Argon lamp. The wavelength coverage of the spectrograph is from 3750 to

9200 Å, with a resolving power of about $R= 50\,000$ and spectral sampling 2.4 Å/mm [2] accessed September 20, 2021.

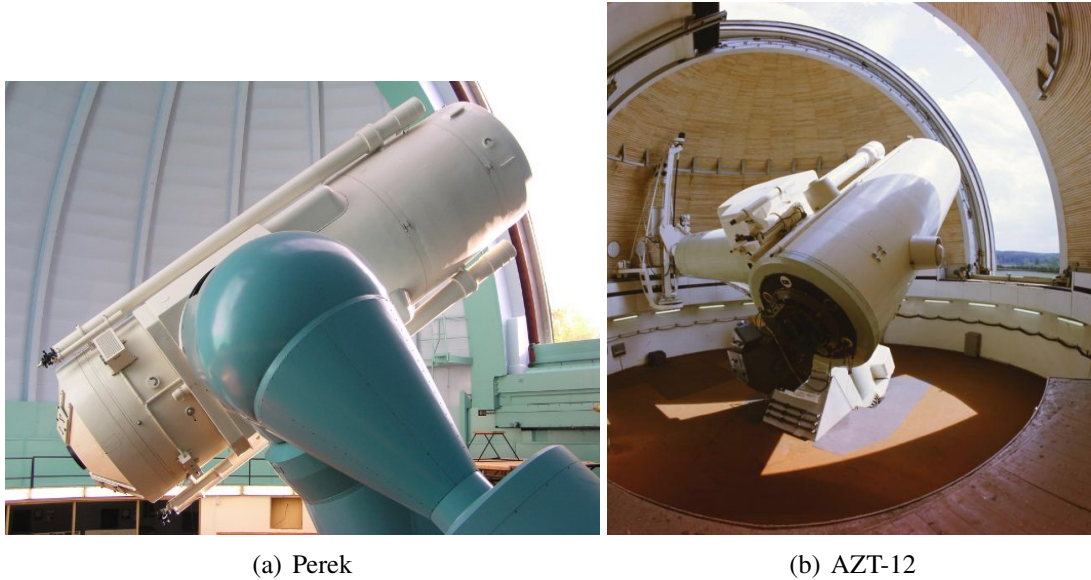


Figure 2.1: Photos of (a) Perek 2-m telescope and (taken from [9] accessed November 30, 2021) and (b) AZT-12 1.5-m telescope (taken from [6] accessed November 11, 2021).

D700 Spectrograph

Single order spectrograph or D700 spectrograph is also (as OES) fibre-fed spectrograph with medium resolution ($R\approx 13000$). It is working in two spectral orders, the first one is going from green to near IR with wavelength coverage $5100 - 8900\text{ Å}$ and the second order from near UV to blue covers the range $4000 - 5100\text{ Å}$. Spectral range is covering $\sim 500\text{ Å}$ adjustable by grating rotation. For data in this study the angle 30.25° was used. Resulting spectrum then cover the range from 6263.5 Å to 6736.0 Å . The spectrograph is completed with detector PyLoN $2048\times 512\text{ BX}$ with liquid nitrogen-cooled working temperature -115°C . (Slechta and Skoda 2002, [7] accessed Mars 18, 2022)

Longslit Spectrograph ASP-32

In the time of mid-80, the AZT-12 telescope was equipped with the long-slit spectrograph ASP-32. The spectrograph is attached directly to the Cassegrain focus and it moves together with the telescope which brings also some disadvantages of taking comparison frames (they must be taken in each position of the telescope). With 10 gratings it can cover the range from 3000 to $11\,000\text{ Å}$. Its detector is thermoelectrically cooled to -90°C . [5] accessed November 7, 2021

2.2 Data Reduction

Data reduction of ASP-32 spectra and OES spectra was done using Image Reduction and Analysis Facility (IRAF) software, while reduction of D700 spectra was performed using IDL-based package, which includes all standard steps which are discussed in the following section.

2.2.1 Data Reduction in IRAF

The IRAF is a software designed for scientific data reduction and analysis using a command-line interface. It is a product of National Optical Astronomy Observatories and was mainly developed for astronomers but later on has been found as a useful tool for general image processing across different branches.

Due to obtaining data via charge-coupled device (CCD) and of course, the observation is taken from Earth, the raw data includes some defects such as bad pixels, pixels with different sensitivity, noise from electronics, cosmic rays, etc., and those flaws must be removed before further analysis.

Cosmic ray removal and bad pixels correction

The very first step is to remove pixels that were saturated by the impact of high-energy particles. Because obtaining spectra of weak targets takes a long time, it is necessary to clear those frames from pixels that are not affected by the star itself. In the final image emission lines which aren't natural to the object may appear. In the case of OES spectra, the cosmic rays correction is done only with bias, flat, and object frames. Comparison frames can be damaged by this step. As it is seen in Fig. 2.2 some lines used for wavelength calibration may be deleted. This step was partially done in IRAF, most cosmic rays were subtracted via DCR freely available from [here](#).

As it is seen in Fig. 2.4 panel (a) some columns or even single pixels are bad, in the way to fix that the 'badpixel mask' (basic text file with a list of known bad pixels or columns) is applied on all frames.

Although frames from OES and ASP-32 are visually different, proceeding steps are very similar. The advantage is that raw frames taken by ASP-32 (in Fig. 2.3) do not cover such an area as echellograms, which means that there is a lower probability to be attacked by high-energy particles. So for that reason only object frames with exposure time ≥ 600 s are corrected for cosmic rays.

Bias combine and correction

Bias is a frame with zero exposure time which reflects noise from electronics.

Usually, 10 or more bias frames are taken during one observation. From bias data sets only good ones (selection is done according to standard deviation and visual comparison) are used for further reduction. Most important is the stability of all frames. Since we have a satisfactory set of biases, they are averaged. The result produces 'masterbias' frame which is used for further reduction. During this procedure, bad pixels are deleted.

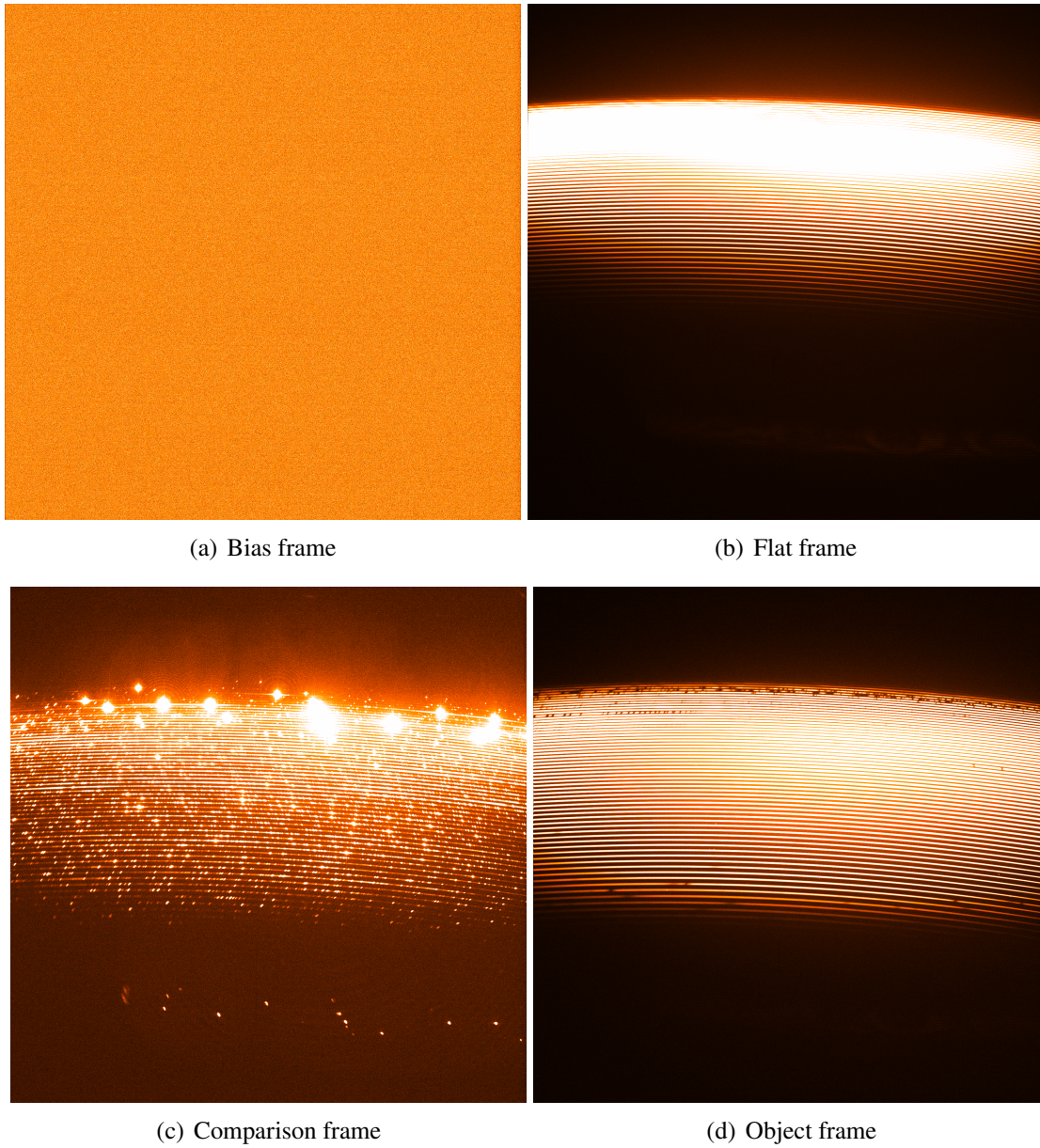


Figure 2.2: Panels (a), (b), (c) shown frames which are used for calibration. Right bottom panel (d) is an example echellogram of HD 21389.

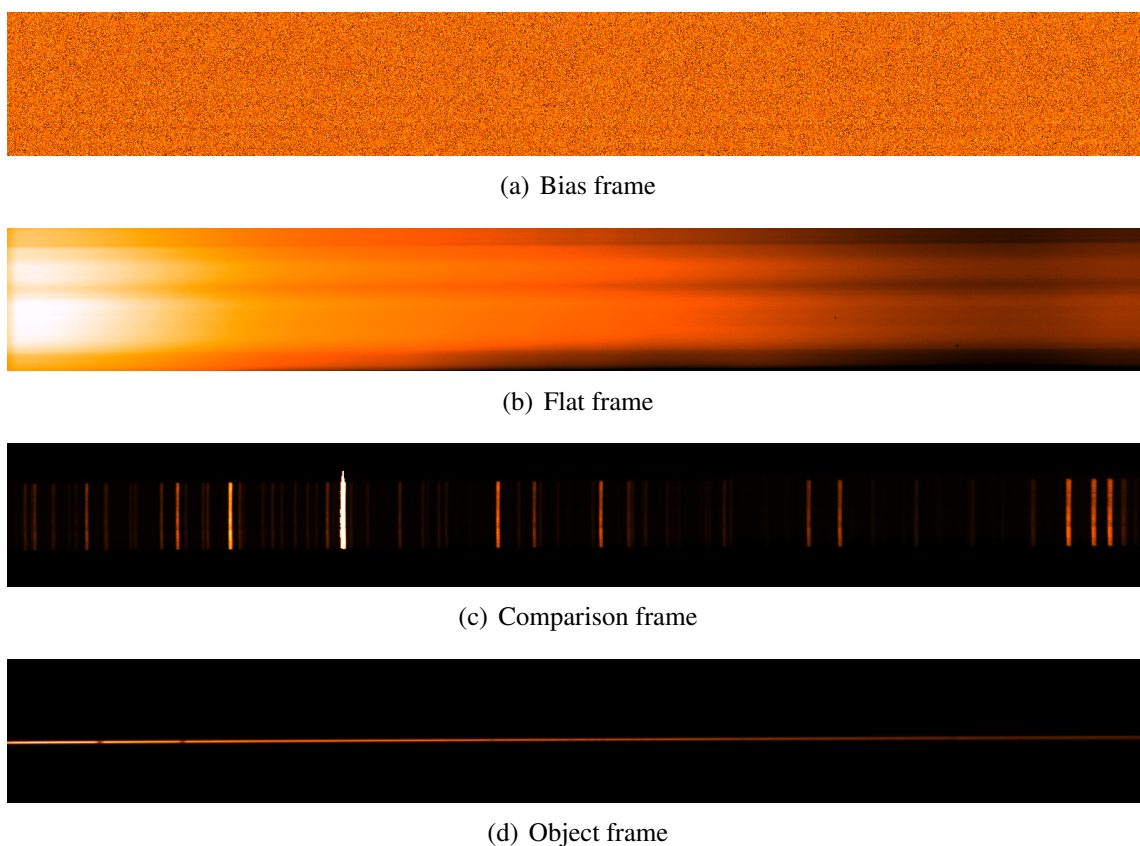


Figure 2.3: Panels (a), (b), (c) shown frames which are used for calibration. Bottom panel (d) is an example raw longslit spectra of HD 21389.

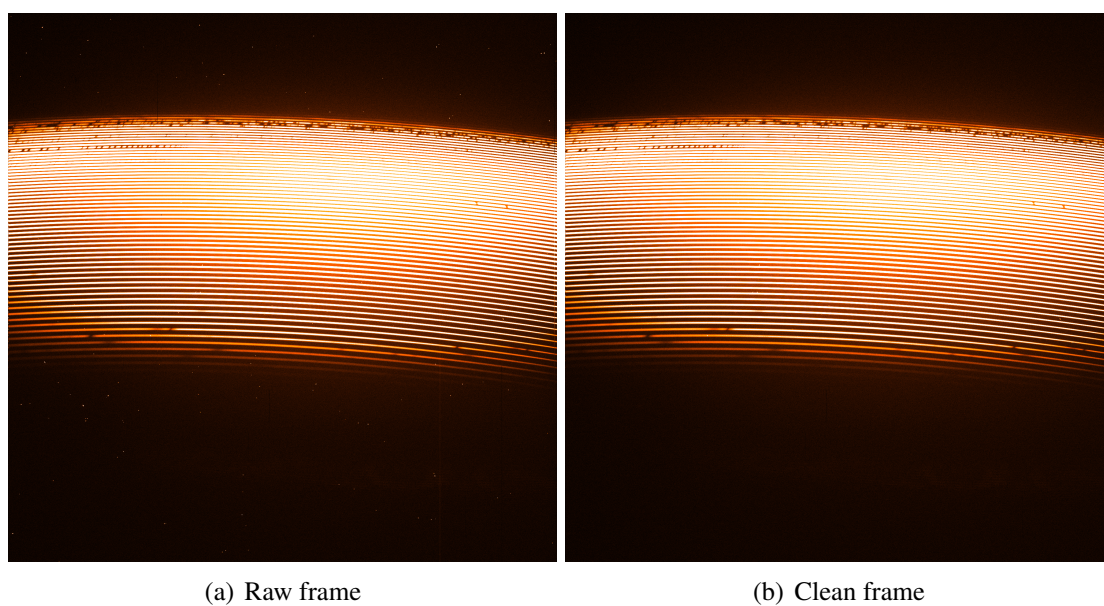


Figure 2.4: Panel (a) shows raw object frame while panel (b) is the same frame after cosmic rays and bad pixels correction. Frames were taken by OES.

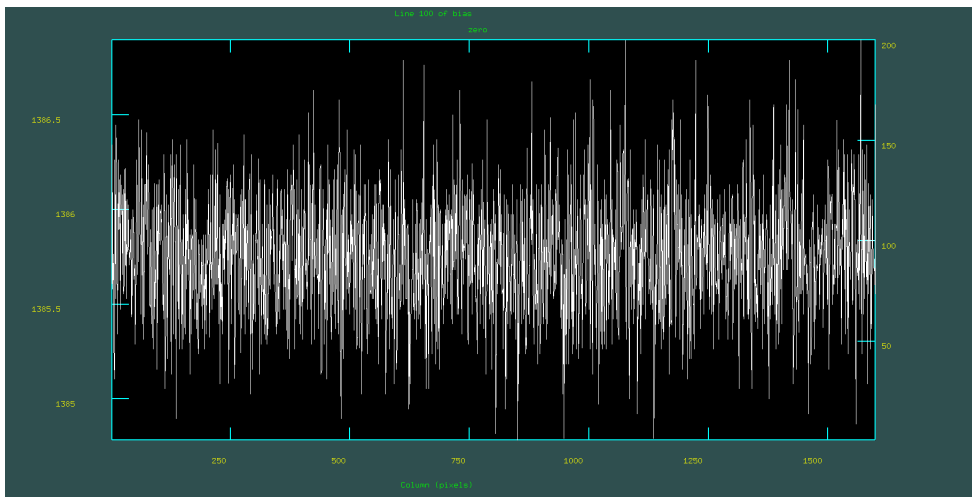


Figure 2.5: Master bias frame viewed in IRAF.

Flat Correction

As same as biases the flat frames are used for calibration. In general, each pixel can be differently sensitive to light and flat correction is used to set equal responsibility of all pixels to a light source with the same flux.

Flats are taken for each grating and grating angle dependent on the observational schedule. By applying median filtering all flat frames are averaged into one resulting 'masterflat' frame.

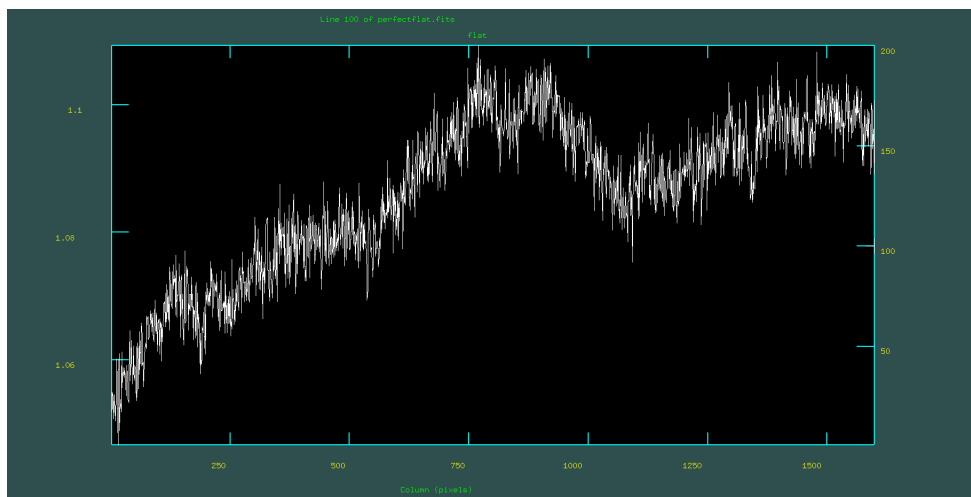


Figure 2.6: Perfect flat frame viewed in IRAF.

Stellar Spectra Extraction

This step aims to suppress background noise and pull out as much of the stellar spectrum as it is possible.

The long-slit spectra include only one aperture which allows us to play around with background noise and the real signal from investigated object.

In the echellogram, the apertures are close to each other which complicates the background suppression. This step includes only marking apertures one by one and fitting them one by one. For this thesis, 49 apertures were extracted.

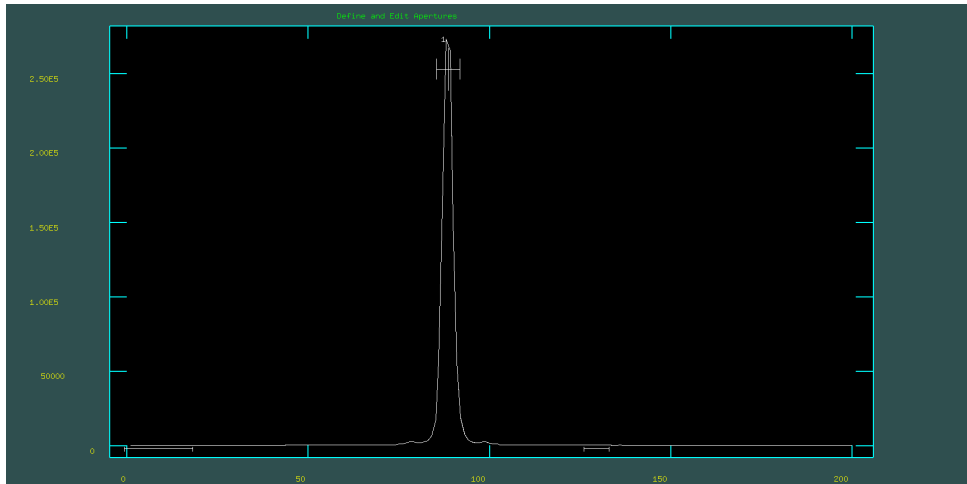


Figure 2.7: Defining aperture.

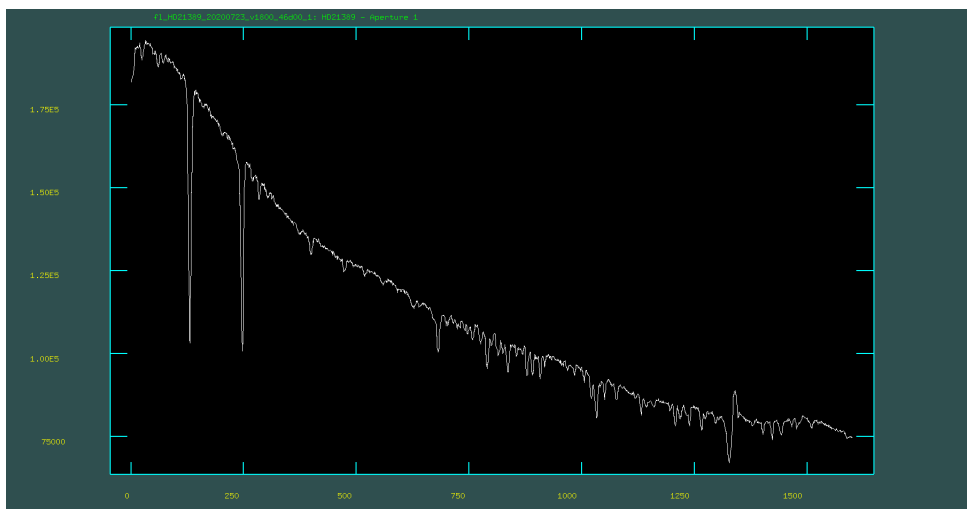


Figure 2.8: Aperture extraction (still in pixels).

Lamp Spectra Extraction, Line Identification and Wavelength Calibration

Frames are taken by a CCD camera which means that all raw images are in pixels. To assign pixels with wavelength we need to identify lines in comparison lamp spectra. Identified lines are fitted by a curve which then determines the distribution of wavelengths along with the entire image.

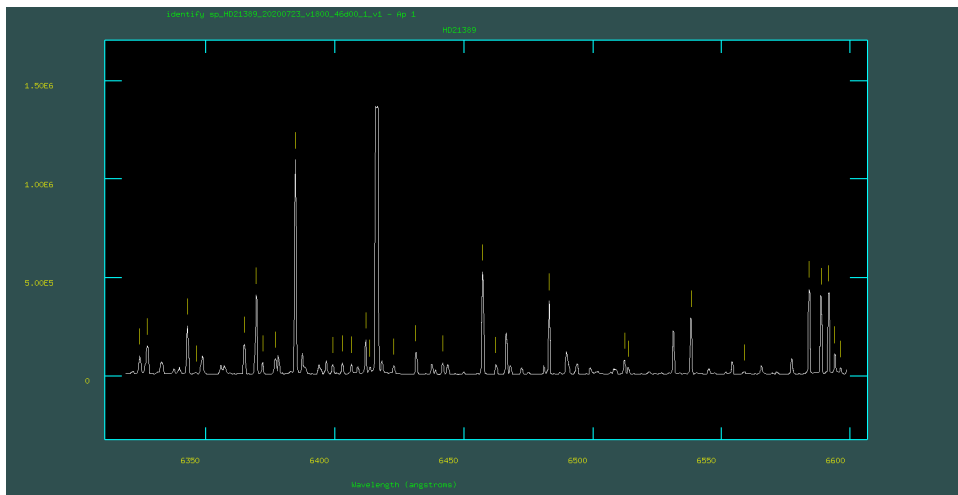


Figure 2.9: Line identification in lamp spectra.

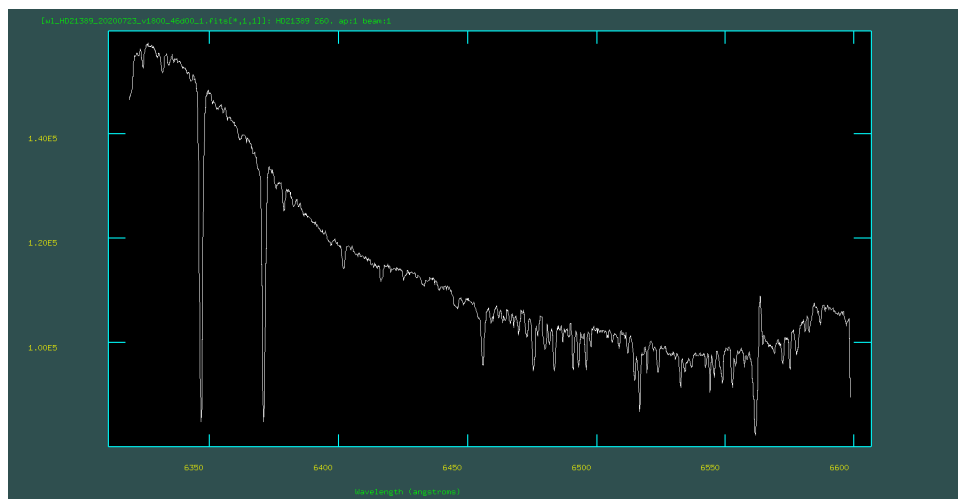


Figure 2.10: Wavelength calibrated spectrum.

2.3 Additional Procedures

2.3.1 Telluric Correction

Since the observation is taken from Earth, spectral data contain an imprint of the Earth's atmosphere in the form of absorption lines of elements present in it. They are relatively narrow due to cool atmospheric gases. Their presence is prevalent in the optical and infrared (IR) part of stellar spectra. Absorption mostly by ozone O_3 , gaseous oxygen O_2 , carbon dioxide CO_2 and water vapour H_2O dominates. Where the lines caused by H_2O demonstrate complexity because they vary with air mass and humidity in the atmosphere. Therefore all observations have specific telluric features regarding the weather conditions at that moment (S. Adelman, Gulliver, and Smalley 2003; Lallement et al. 1993).

The main goal of this thesis is to describe the variability of $H\alpha$ line. As it is seen in 2.11 the region around $H\alpha$ is strongly affected by atmospheric lines so that is why all spectra from Ondřejov were cleaned from telluric lines via MOLECFIT 1.5.1. software. It has been developed for European South Observatory (ESO) by a team of astronomers at the Institute for Astrophysics and Particle Physics at the University of Innsbruck. Molecfit is a powerful tool used to correct astronomical observations for atmospheric absorption lines. Based on a given observatory's climate, local meteorological data from fits-header, and dynamically retrieved altitude profiles for temperature, pressure, and humidity it creates synthetic transmission spectra which are then fitted to the observational data.

The efficiency of telluric correction deserves a discussion, in some spectra telluric remnants are still presented and as it is seen in Fig.2.11 it highly affects the region of broad emission wings around $H\alpha$ line.

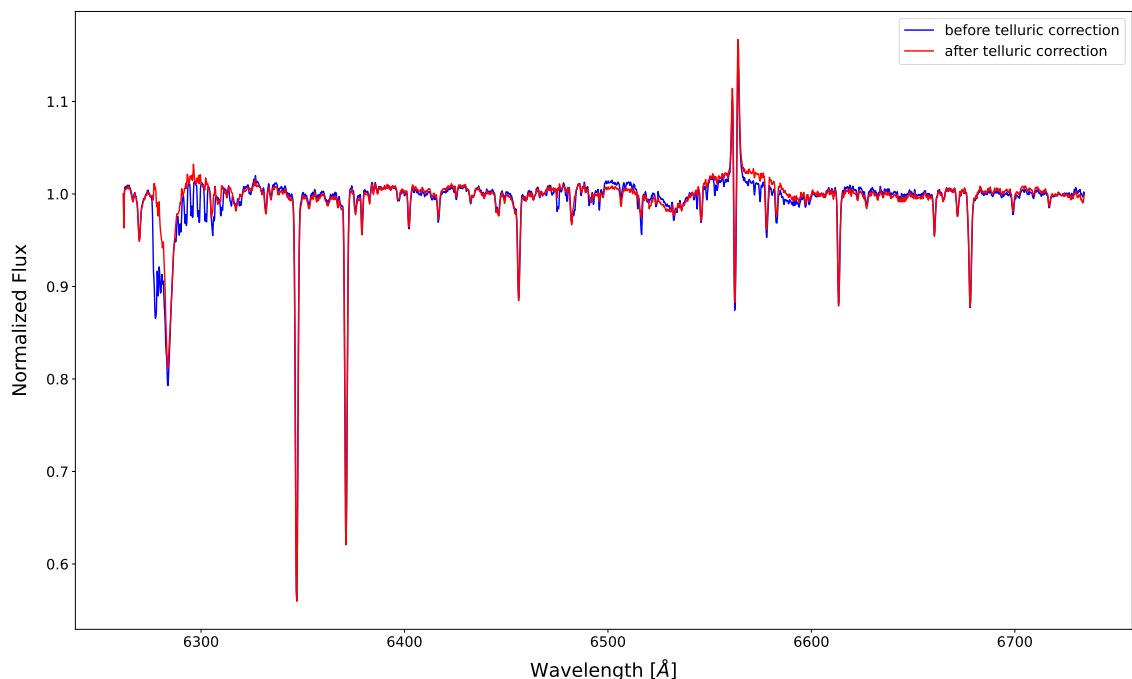


Figure 2.11: Comparison of spectra obtained on 2017 Dec 7th before and after telluric correction.

2.3.2 Velocity Correction

Each observation needs to be corrected for the motion of the observer in direction of an observed target because the Earth does not have a fixed position in space. The correction has to be taken concerning the fixed point - barycenter. (Earth rotation, Earth moves around Earth-Moon center, the motion of Earth-Moon center around the Sun and in the end, also Sun is moving around a center of the solar system which is known as barycenter).

All spectra were corrected for velocity out of IRAF using a procedure written in Python or IDL (their accuracy is comparable) because IRAF can only calculate a heliocentric correction. The sample code for velocity correction is shown in Appendix.

2.3.3 Normalization

The normalization was carried out with the IRAF task. The very last step of spectral data reduction is normalization. The curved spectrum is fitted and aligned with the continuum. Because normalization is the most influenced by subjective feeling, this step is shown to be very crucial for maintaining the extended emission wings which are present around the Balmer lines.

This feature presented around $H\alpha$ especially complicates the normalization. The wings are split into two apertures in OES spectra and therefore is not possible to normalize them correctly. The same problem with the normalization is in the case of spectra obtained at Tartu Observatory. The edge of the frame corresponds to the end of the emission wings. And because no endpoint could be assigned with continuum level, they were normalized so that the wings disappeared.

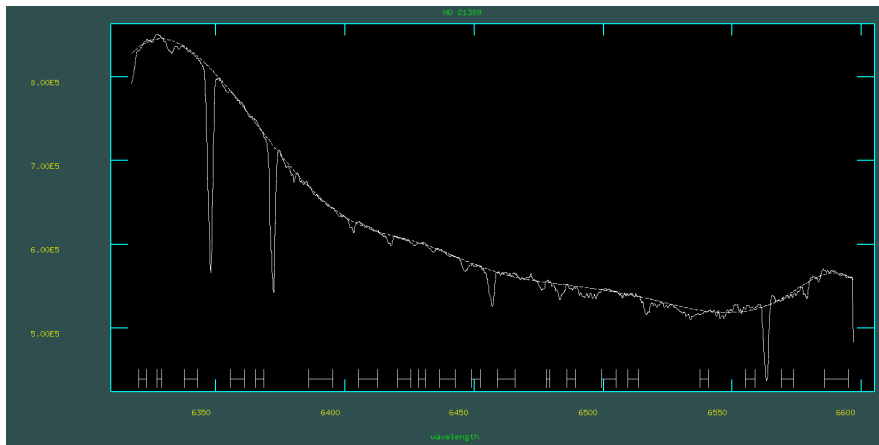


Figure 2.12: Normalization of wavelength calibrated spectrum.

2.3.4 Reduction of OES Spectra

For OES data was developed a script `oesred.cl` which makes reduction much easier. The script is designed by M.Sc. Mauricio Cabezas who is a researcher at Ondřejov Observatory. More information about the script itself and each reduction step are available [here](#).

Needed to note that previous paragraphs are related to long-slit spectra reduction. On the other hand proceeding of echelle spectra consist of the same steps. First of all cosmic rays and bad pixels are deleted. For OES spectra the cosmic rays correction is not as efficient as it is in the case of long-slit spectra. Because instead of just one the OES spectra contain multiple apertures placed just above each other (Fig.2.2). The following steps are master bias and master flat creation. Modeled aperture is made on master flat image and then used to define apertures in Th-Ar comparison lamp frame and object frame. When the model aperture of the comparison spectrum is done individual spectral lines must be

identified. Then all apertures are corrected for master bias and flat fielded. This is usually followed by heliocentric velocity correction and additionally, the julian date is written in the header. Each aperture in pixels before is calibrated now to wavelength scale. In the end, all normalized apertures are merged in the resulting spectrum which has to be corrected for barycentric velocity (in our case out of IRAF). A detailed description of OES spectra proceeding via IRAF can be found [here](#).

Chapter 3

Spectral Variability Analysis

This study includes 92 spectra of HD 21389 from which 52 were acquired by Single order spectrograph (D700) in $H\alpha$ region, 30 of them were obtained by long-slit spectrograph ASP-32 also in $H\alpha$ region and the last 10 were obtained with OES in a range from $\sim 3964 \text{ \AA}$ to $\sim 8738 \text{ \AA}$.

In this work, we focused on the study of the variability of $H\alpha$ line profiles, as well as on the measurement of radial velocities of absorption spectral lines to test the possible binarity of the star and trace the motion of matter in its atmosphere. For that, the lines listed in Tab. 3.1 were selected.

Table 3.1: List of spectral lines of which the radial velocities were measured (λ is air wavelength).

Sp. line	λ [\AA]	D700	ASP-32	OES	Sp. line	λ [\AA]	D700	ASP-32	OES
Si II	6347.11	✓	✓	✓	DIB	6613.56	✓		
Si II	6371.37	✓	✓	✓	DIB	6660.64	✓		
Fe II	6456.38	✓	✓	✓	$H\beta$	4861.32			✓
Mg II	6545.94	✓	✓	✓	$H\gamma$	4340.46			✓
$H\alpha$	6562.80	✓	✓	✓	$H\delta$	4101.73			✓
C II	6578.05	✓		✓	Na I	5889.95			✓
C II	6582.88	✓		✓	Na I	5895.92			✓
He I	6678.15	✓		✓					

There is a systematic distinction between the spectra acquired by two different spectrographs used in this work – D700 of Ondřejov Observatory and ASP-32 of Tartu Observatory. As the discussion of these differences is outside the scope of this work, we will consider these data separately, and will not compare the radial velocities acquired by different instruments.

Before the results of its spectral variability will be presented, the process of measuring radial velocities and some additional steps of data reduction should be mentioned. Due to the lines' profiles often being asymmetric the radial velocities were measured using the

program reSpefo (Harmanec 2022). reSpefo is the program for one-dimensional spectra analysis, upgraded version of SPEFO (Skoda 1996), freely available [here](#). Instead of line profile fitting the mirrored line profile is used (as it is seen in Fig. 3.1) for radial velocities measurement. In addition to the measurement of radial velocities, the program also allows the measurement of equivalent widths and to do spectrum normalization.

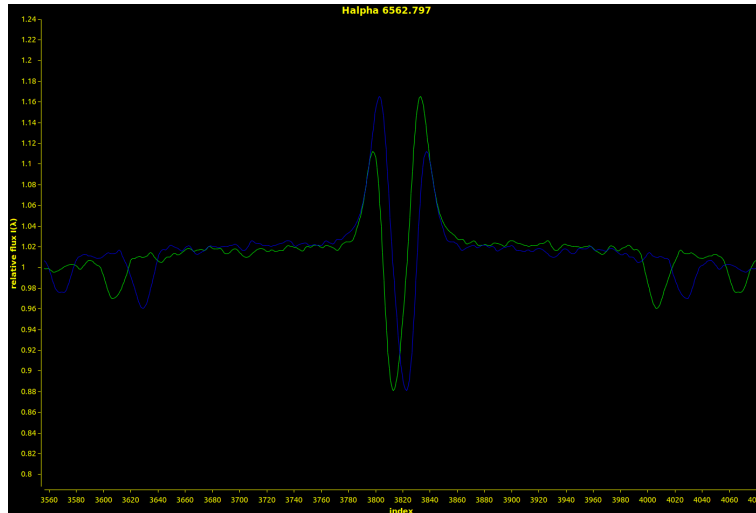


Figure 3.1: Sample image from measurement of radial velocities via reSpefo.

3.1 DIB Lines Correction

The diffuse interstellar bands (DIBs), are absorption features observed in stellar spectra in the infrared, optical, and ultraviolet region. The origin of most DIBs remains unknown, with common suggestions being polycyclic aromatic hydrocarbons and other large carbon-bearing molecules. They are prominently broader than other atomic interstellar lines. Equivalent widths of DIBs may be used for measurements of interstellar reddening $E(B - V)$ (Friedman et al. 2011). Due to their interstellar nature, they are not affected by Doppler shifting, thanks to which they may be also used to verify the stability of the spectrograph and correctness of the data reduction process.

At the beginning of 2020, the Perek's 2-m telescope underwent a reconstruction. Since that time the light has been traveled to spectrographs through an optical fiber. As it is seen in Fig. 3.2 after the reconstruction the estimated radial velocities of DIB lines became more scattered.

We can exclude the effect of estimation of radial velocities despite the line profile is in some spectra more asymmetric because all lines were measured the same way. Maybe something went wrong during the processing or it comes from instrumental settings, anyway particular study of these effects is outside the scope of this study. Later on, the normalization was examined as a possible source of scattering and even though the parameters of fitted polynomials are different, the results are not affected by this proceeding step.

For this reason, the data taken from 2020 up to now have been corrected by a shift in the DIB lines. Averaged value of radial velocities in DIB lines measured from 2017 to 2019 ($\bar{v}(DIB)$) was taken as a standard - Eq.3.1. Than all estimated radial velocities of DIB lines ($v_i(DIB)$) from the beginning of 2020 were compared to the average value using Eq. 3.2 and rest of spectral lines ($v_{estimated}(line)$) have been corrected according to Eq. 3.3 for that deviation (Δv).

$$\bar{v}(DIB) = \frac{\sum_1^n v_i(DIB)}{n} \quad (3.1)$$

$$\Delta v = v_i(DIB) - \bar{v}(DIB) \quad (3.2)$$

$$v_{corrected}(line) = v_{estimated}(line) - \Delta v \quad (3.3)$$

And for comparison radial velocities estimated from OES spectra were added into figures made up of data from D700. At least radial velocities measured from OES and D700 spectra (after the correction) taken during the same observational night show very similar values.

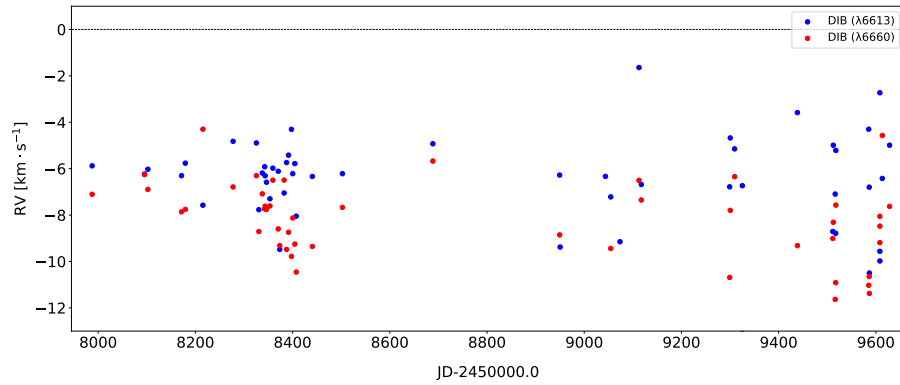


Figure 3.2: Radial velocities DIB lines ($\lambda 6613; 6660$) measured from spectra obtained with D700 spectrograph. Data were used for instability correction.

3.2 Telluric Correction

The telluric correction was mentioned in Chapter 2.2.1 as one of the procedure steps. Later on, it turns out that telluric correction artificially affected the spectrum which is the most significant around $H\alpha$ line. All data and figures in this study are estimated from spectra after telluric correction except the Fig. 3.8. As it is seen in Fig. 2.11 the broad wings are shifted, so this is only part made up of not corrected spectra. Just to be sure about 'How much does the correction damage the original frames?' I went through the spectra showing specific details such as very deep absorption component or multiple components and it certainly doesn't look like the correction would cause the shift of line centers. In the case of some weaker lines for example C II lines next to the $H\alpha$ their flux may differ, but in this study, only radial velocities of line cores were measured.

3.3 Spectrum of HD 21389

According to the original Harvard classification which is based predominantly on hydrogen lines, they reach the largest strength in spectra of A-type stars. For A-type supergiants, the hydrogen lines are noticeably strong and have maximum strength for A0 ones. The spectrum of HD 21389 is in agreement with its spectral classification (A0 Ia) – in the spectrum, the strong Balmer lines are visible. Moreover, $H\alpha$ line sporadically shows an emission asymmetric profile, which is evidence of stellar wind and extended stellar atmosphere. Other Balmer lines are observed in absorption with asymmetric profiles too. In the spectrum of HD 21389 many spectral lines of neutral and ionized metals (eg. Mg, Fe, Ca, Ti) are visible, especially the strong doublet of Si II (λ 6347, 6371). Weak C, O, and N lines are also presented.

Except for the lines intrinsic to the star the spectrum contains an imprint of Earth's atmosphere in form of telluric lines and lines coming from the interstellar environment (DIBs, Na I D - usually saturated, Ca II).

The results of line identification (air wavelength) are shown in Appendix: Fig. 4.25 - Fig. 4.33.

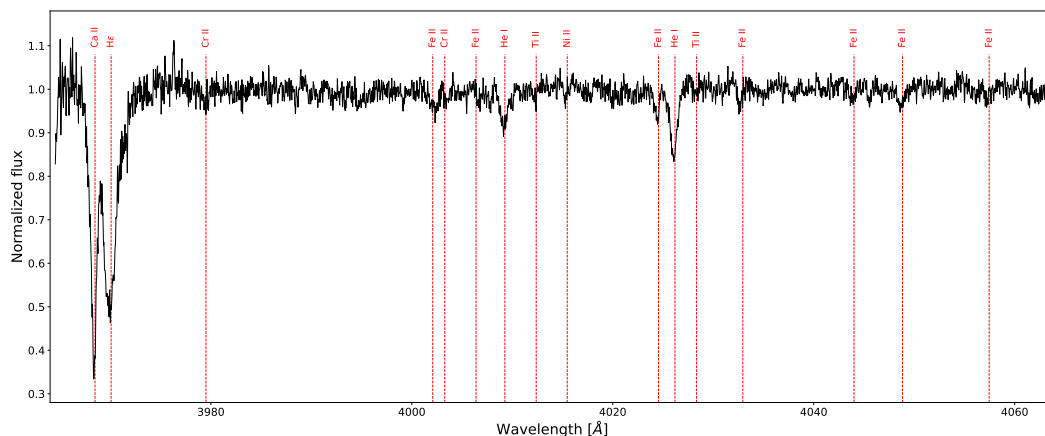


Figure 3.3: Spectrum of HD 21389 in H ϵ region.

There is no evidence for strong emission lines (occasionally the $H\alpha$ line in emission is observed). Sometimes a few weak emission lines appear, but these are artifacts remaining impacts of high-energy particles on the CCD camera chip which survived the cosmic rays correction.

3.4 Variability in $H\alpha$ line

It is known that $H\alpha$ line is the best indicator of stellar wind in B- and A-type supergiants (eg. de Jager 1984; Ebbets 1982), because it is formed in upper layers of the atmosphere where also the base of stellar wind takes place, and HD 21389 with its strong variability in $H\alpha$ (e.g. Aydin 1972; Denizman and Hack 1988; Verdugo, Talavera, and Gómez de Castro 1999a,b) is no exception.

Fig. 4.23 and Fig. 4.24 show $H\alpha$ line profiles obtained with D700 and ASP-32 spectrographs. $H\alpha$ line has a complex structure and reveals rapid variability across the whole data set with not that significant changes on a time scale of several hours. Pure absorption, normal and inverse P Cyg, and three-component shape (central absorption with emission on both sides) profiles were observed. Sometimes (e.g. 2018-08-10, 2019-07-27, 2019-08-16) highly asymmetric profiles appear or profiles where the absorption component is above the continuum level (e.g. 2020-11-03).

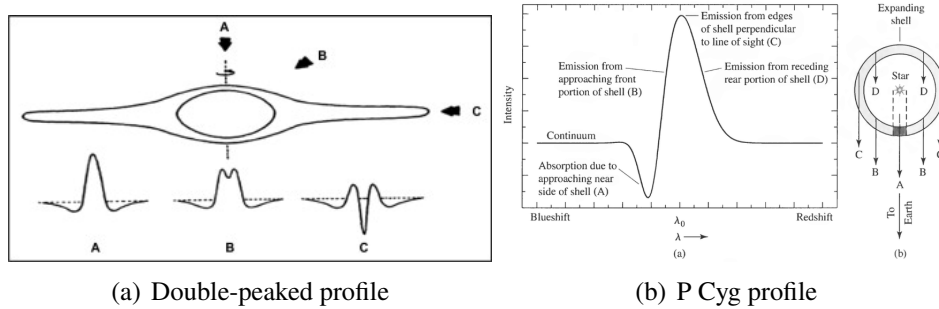


Figure 3.4: Panel (a) shows different points of view and corresponding appearance of double-peaked line profile. Taken from Saad, Hamdy, and Abolazm 2012. While panel (b) demonstrates the formation of P Cyg line profile. Taken from Kasai 2013.

Fig. 3.4 shows schematically how the P Cyg profiles form, and the appearance of double-peaked profile depending on our point of view. The P Cyg profile is a combination of red-shifted absorption and blue-shifted emission component which is caused by outflowing material. Absorption features arise in matter moving toward the observer or away from us, while the emission component is produced in its expanding envelope. For inverse P Cyg profile the emission feature is blue-shifted and the absorption part is transferred to the longer wavelength. Double-peaked emission is an indicator of an extended gaseous shell around the star with an equatorial ring or disk-like structure that is oriented close to the line of sight at the moment of observation. On the other hand, this fact alone cannot be taken as proof, this profile may form in some specific configurations in the circumstellar matter.

Fig. 4.22 and Fig. 3.5 present data obtained with D700 spectrograph as dynamic spectra (in whole – 2017-2022 and in part – July - October 2018). The dynamical spectrum provides an overview of stellar wind behavior in time and the line profile series gives us a more detailed view of each individual.

In other spectra (OES spectra and spectra from the Tartu Observatory) the end of the emission wings corresponds to the edge of the frame, therefore it is not possible to normalize them properly. Thus the flux would not correspond to reality and that is why dynamic spectra are not shown there.

The cycle of changes revealed by $H\alpha$ line is somehow predictable (Fig. 4.24 and Fig. 4.23), concretely inverse P Cyg was never observed to arise directly from pure absorption. The double-peak profile appears from P Cyg and transforms smoothly back to P Cyg. When the pure absorption is seen, in near future (the latest after a month) will be observed in P Cyg which is occasionally transferred into inverse P Cyg, or double-peaked profile.

Sometimes highly asymmetric profiles appear, but it is intermittent, and in general, based only on lines' profile time sequence unpredictable. The observed cycle is consistent with what is suggested by Zeinalov and Rzaev 1990b – absorption profile goes to P Cyg and it changes to an inverse P Cyg profile, finally it turns back to pure absorption. However, it is worth noting that conclusions by *ibid.* are based on significantly fewer observations, and they did not register a double-peak profile at all.

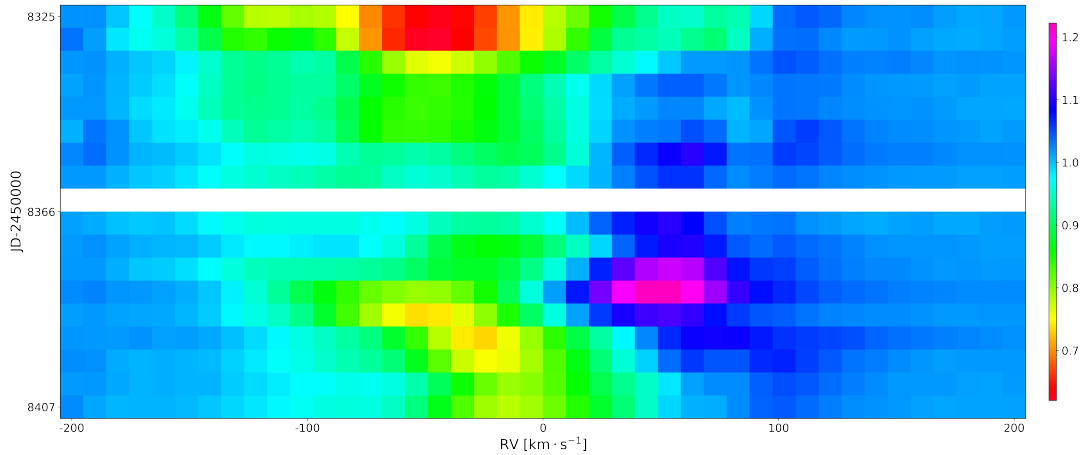


Figure 3.5: Cut part of Fig. 4.22 (in Appendix) - dynamical spectrum of $H\alpha$ region intercepting possible final phase of HVA event.

According to our data during July 2018 HD 21389 underwent high-velocity absorption (HVA) event, which reached its end in August 2018. In Fig. 3.5 the event corresponds to slices with the reddest parts (~ 0.6 continuum intensity). The absorption components were observed with highly negative velocity about $-50 \text{ km} \cdot \text{s}^{-1}$ (Tab. 3.3 and Tab. 3.4). In 1993 and 1994 these events were observed and described by Corliss, Nancy D. Morrison, and S. J. Adelman 2015. The intensity reached ~ 0.4 and ~ 0.6 of continuum level in the most active phase of the event. The presence of HVA events in HD 21389 was confirmed also by Richardson et al. 2011.

$H\alpha$ line of B- and A-type supergiants occasionally shows blue-shifted and deep absorption components. It was already observed in a few stars HD 91619 (B7 Iae), HD 96919 (B9 Iae), HD 34085 (B8 Iae), and HD 199478 (B8 Iae) by Kaufer, Stahl, Wolf, Gaeng, Gummersbach, Jankovics, et al. 1996; Kaufer, Stahl, Wolf, Gaeng, Gummersbach, Kovacs, et al. 1996; Markova et al. 2008; N. D. Morrison, Rother, and Kurschat 2008, while HD 21389 belongs to those in which it was observed. Corliss, Nancy D. Morrison, and S. J. Adelman 2015 have been analyzed 152 spectra obtained from 1993 through 2007 and found that between 1993 and 1994 high-velocity absorption (HVA) events were observed in the atmosphere of HD 21389.

These events are reported on a time scale from tens of days to several months (Markova et al. 2008). Active phases with observable high-velocity absorption (HVA) events are associated with significant variability in $H\alpha$ line while more quiet phases do not include HVA events and present less variability (Corliss, Nancy D. Morrison, and S. J. Adelman 2015). Israelian, Chentsov, and Musaev 1997 suggests magnetic field as a source of this behavior. Magnetic spots at the stellar surface may lead to the creation of magnetically

supported material loops in the wind surrounding. While the velocity fields and density differ from a stellar surface such a loop can be created and may give rise to HVA events. This possible explanation is also supported by Markova et al. 2008.

3.4.1 Broad Emission Wings around Balmer Lines

During the analysis of the $H\alpha$ region, the extended wings were found (Fig. 3.6 - third window). After the reduction of OES spectra was finished it turned out that broad wings are presented around other Balmer lines, not only around $H\alpha$. The presence of an extended wing is confirmed with archive spectrum obtained in 1995 with a 1.93m telescope of Observatory de Haute Provence ([8] accessed November 30, 2021) and spectra obtained at Tartu Observatory in Estonia.

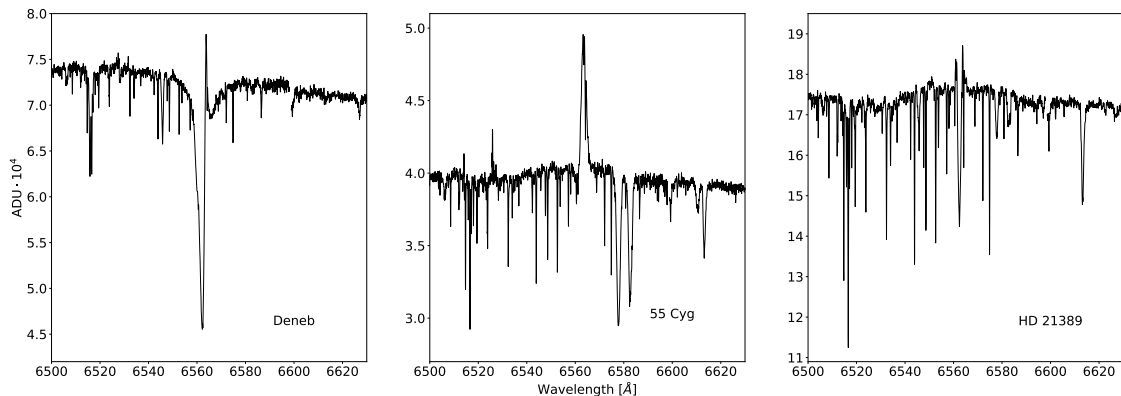


Figure 3.6: The first, second and third window show spectra of Deneb, 55 Cyg and HD 21389 in order. All of them were taken from [8] accessed November 30, 2021.

Kaufer, Stahl, Wolf, Gaeng, Gummersbach, Kovacs, et al. 1996 investigated six late B and early A-type supergiants. All of them except α Cyg have been observed with broad emission wings around $H\alpha$ extended to about $\pm 1200 \text{ km} \cdot \text{s}^{-1}$. Fig. 3.6 shows the $H\alpha$ region of three stars (α Cyg, 55 Cyg, HD 21389), which belongs to α Cyg type variables with Deneb as their prototype. For HD 21389 as for 55 Cyg the feature is prominent, while for α Cyg if the wings are there, they are very weak.

According to a study by Ebbets 1980, extended wings are symmetric and stable in time. This phenomenon was studied in O and B supergiants such as α Cam, 55 Cyg, κ Cas, and many more. A study published two years later (Ebbets 1982) reports variability of extended wings on a time scale of years. Although our measurement revealed some kind of variability depending on the shape of the line core, which is more of a matter of days. The measured extent of wings is about $\pm 1500 \text{ km} \cdot \text{s}^{-1}$ (Fig. 3.7 panel (a)) while by Kraus et al. 2015 reported extent for star 55 Cyg of B4 Ia spectral class is $\pm 1200 \text{ km} \cdot \text{s}^{-1}$. It is needed to noted that spectra of both objects were obtained with same instrument – D700 spectrograph in Ondřejov.

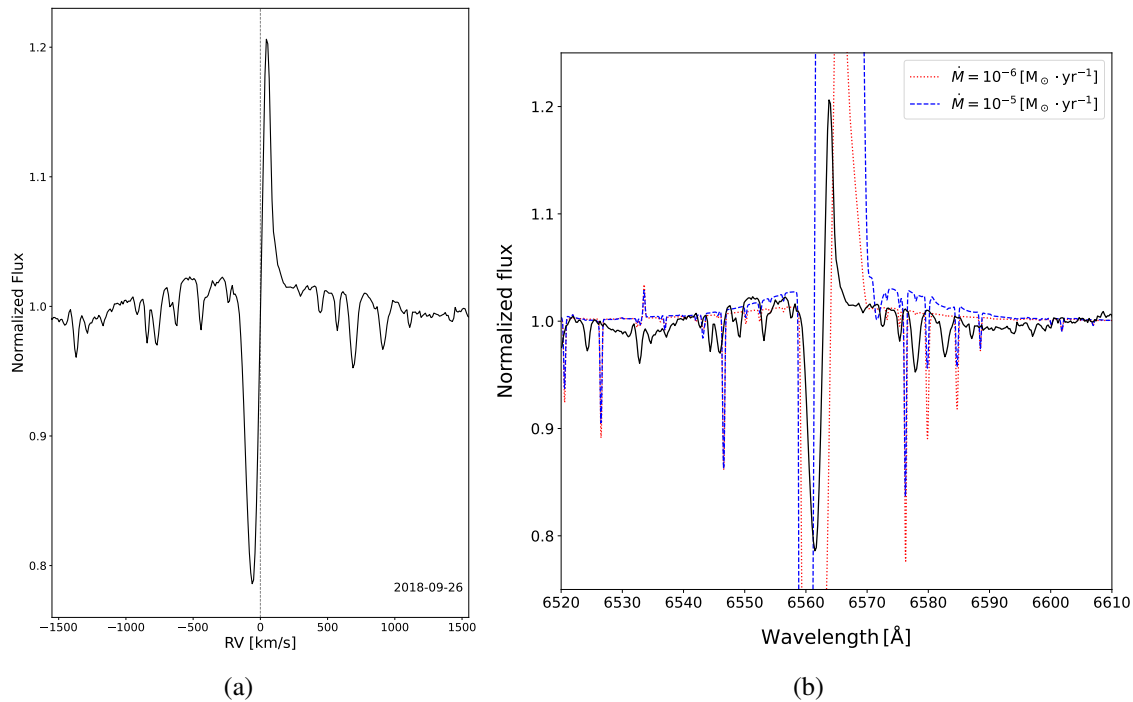


Figure 3.7: (a) Extended wings around H α in spectrum HD 21389 in velocity units. (b) Comparison of observed and modeled CMFGEN spectra. Black is the real spectrum of HD 21389, while the red dashed and blue dotted (higher mass loss) are modeled spectra for A-type supergiants with different mass loss.

Despite the spectra of HD 21389 having been studied before and especially the H α region, no one has mentioned this phenomenon with this star. Stars 55 Cyg, α Cam and κ Cas were observed with broad emission wings which occasionally completely disappear in the study by Ebbets 1982 and in spectra obtained in Ondřejov. For HD 21389 no disappearance of broad wings has been recorded. In all spectra used for this study extended wings are visible and are also presented in spectra obtained with ELODIE on 1995 Nov 11 (Fig. 3.6 - third window). So the fact that no one has noticed this feature before probably comes from proceedings, particularly normalization, and not from their absence.

The originate of broad emission wings is explained by electron-scattered photons coming from the deep atmospheric layers (eg. Kaufer, Stahl, Wolf, Gaeng, Gummersbach, Kovacs, et al. 1996, McCarthy et al. 1997, Kudritzki et al. 1999).

Fig. 3.7 panel (b) shows a comparison between the observed spectra (black) of HD 21389 and two modeled spectra (red and blue). Models were generated using CMFGEN code with spherical symmetry and initial parameters corresponding to A-type supergiants. Thomson free electron scattering and Rayleigh scattering are included in CMFGEN. However it is inadequate in the case of this star to use spherical symmetry, it is just for illustration that such effects may be observed in spectra of A-type supergiants. For both spectra, the initial conditions are the same except for the \dot{M} .

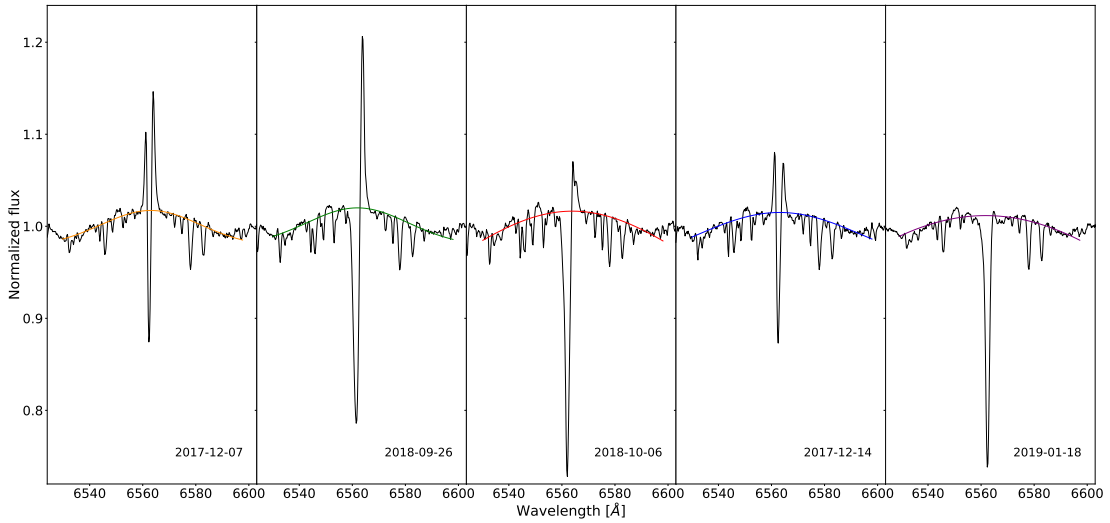


Figure 3.8: Shape of extended wings around H α line fitted by Gaussian profile. Results present correlation between the strength of emission wings and central line profile.

Width Parameter of Gaussian fit					
	2017-12-07	2018-09-26	2018-10-06	2017-12-14	2019-01-18
σ [Å]	18.7	19.2	47.8	32.4	89.1
	± 1.4	± 2.0	± 42.0	± 8.3	± 20.1

Table 3.2: Obtained parameter of Gaussian fit.

The high uncertainty of σ from 2018-10-06 is caused by the method of continuum fitting. Since the region is infected by telluric lines, it is difficult to determine a continuum without having to be manually involved in the process.

To make any conclusion about the nature of the broad wing's variability, more spectra need to be tested.

In the beginning, the hypothesis was to prove or disprove whether the broad wings vary in time. For this reason, the sample of examined spectra was chosen by different central line profiles. Later on, it turned out that highly telluric-affected spectra cannot be properly fitted, so the next selection was done with a requirement on weak telluric lines. The results of fitting are demonstrated in Fig. 3.8 and supported by estimated width parameters in Tab. 3.2. Based on this one can be sure about the variability in time. And this was even confirmed with spectra before the normalization from Ondřejov archive. Broad emission wings in spectra with various H α line profiles taken in two different epochs were visually different. Moreover, the outcome points to a correlation between the strength of the central line profile and the extension of broad wings.

P Cyg profile (second window in Fig. 3.8) arises due to the strong stellar wind. When the wind is weaker, which means that the mass loss decrease, the rotation effect of the circumstellar envelope appears in form of a double-peaked profile (first and fourth window

in Fig. 3.8). And during the 'quiet' phases we observe the absorption profile without any emission component (last window in Fig. 3.8). So when the stellar wind decreases, the effect of scattered photons is stronger. But the question is 'Whether such an effect is real?' still, the correlation might be artificially touched by the fitting..

3.5 Sign of Binary Character

At the beginning of the 20th century, this star was included among the candidates for spectroscopic binaries. That was for the first time and as I know also for the last time when this star was suspected to be a part of a binary system. But maybe this study brings new results.

In Fig. 3.16 and Fig. 3.11 the radial velocities of Mg II (λ 6546) are plotted. While the spectra taken by the D700 spectrograph present mostly negative values, results are a bit different for velocities measured from spectra obtained by ASP-32. Together the data from both spectrographs show periodic structure. The radial velocities vary from $-18 \text{ km} \cdot \text{s}^{-1}$ to $+18 \text{ km} \cdot \text{s}^{-1}$ and do so at repeating intervals after ± 400 days. On the other hand, the period is closed to one year, so the star is in the sky in the same position. Maybe the deformation is related to some specific position of the telescope since it is repeated within one year period when the star is in the same direction in the sky.

Even the observation points to some signs of binary character, we cannot be sure of this, and the changes may be caused by other effects. Together the data from different spectrographs well cover a whole period from 2017 to the beginning of 2022. Unfortunately, it turned out that the data are not so easily comparable.

In the previous section, the nature of variability in broad emission wings around $\text{H}\alpha$ has been discussed. One of the possible causes could be the interaction between the members in the binary system.

3.6 Variability in Other Spectral Lines

Most supergiants exhibit long periodic changes in their spectra, so a long observation is needed to cover the whole period. All programmed lines present asymmetry in lines' profiles. Even Na I D show small variability in lines' profile, but radial velocities are stable. Maharramov and Baloglanov 2015 found for HD 21389 correlation between asymmetry in lines' profile of Na I D, and inverse P Cyg profile of $\text{H}\alpha$ line. It is typical for active phases of its atmosphere and may be associated with the growth of envelope and matter ejection. All line profiles of $\text{H}\alpha$ in our case are blue-shifted in comparison to the first (standard) profile, but none of them has been observed in inverse P Cyg shape (Fig. 3.17).

Example line profiles taken only from OES data are in Fig. 3.18, Fig. 3.17. And most of them show variability in radial velocities. Estimated radial velocities are discussed in separate chapters according to the spectrograph which were taken by. And radial velocities measured in OES spectra were added into figures with data from D700 just to see how efficient the DIB lines correction was.

The radial velocities of different lines give us information on motion in a concrete layer. From Tab. 3.4 the simultaneous contraction and expansion of some layers are seen, which

is associated with the existence of transitional layers placed between.

Contraction is mostly seen in data from Tartu Observatory, data taken by D700 point to deep and moderate expansion.

3.6.1 Data from D700

Measured radial velocities are listed in Tab. 3.3. The accuracy of this spectrograph is about $2\text{ km} \cdot \text{s}^{-1}$, that is the reason why error bars are not included because uncertainty given by the measurement is much lower (about $0.4\text{ km} \cdot \text{s}^{-1}$).

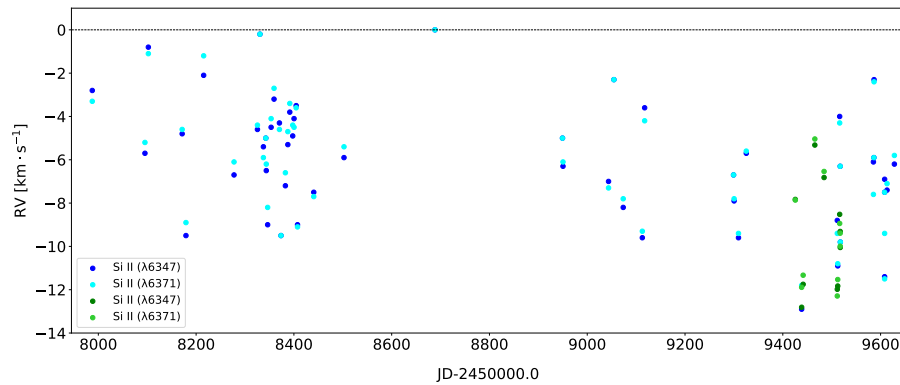


Figure 3.9: Measured radial velocities of two silicon lines Si II ($\lambda 6347, 6371$). Blue dots represent data from D700 and green ones are data from OES.

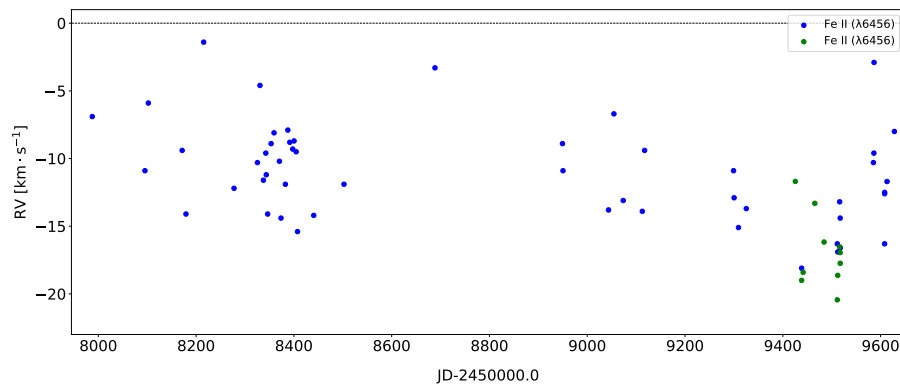


Figure 3.10: Measured radial velocities of iron line Fe II ($\lambda 6456$) - D700. Blue dots represent data from D700 and green ones are data from OES.

Si II ($\lambda 6347, 6371$) vary in radial velocity from $0.0\text{ km} \cdot \text{s}^{-1}$ to $-12.9\text{ km} \cdot \text{s}^{-1}$ (Fig. 3.9).

Analysis of radial velocities of Fe II ($\lambda 6456$) which is seen in Fig. 3.10 does not point to 7.7 day period previously published by Abt 1957, for that more frequent observation would be required. It vary from $-1.4\text{ km} \cdot \text{s}^{-1}$ to $-18.1\text{ km} \cdot \text{s}^{-1}$.

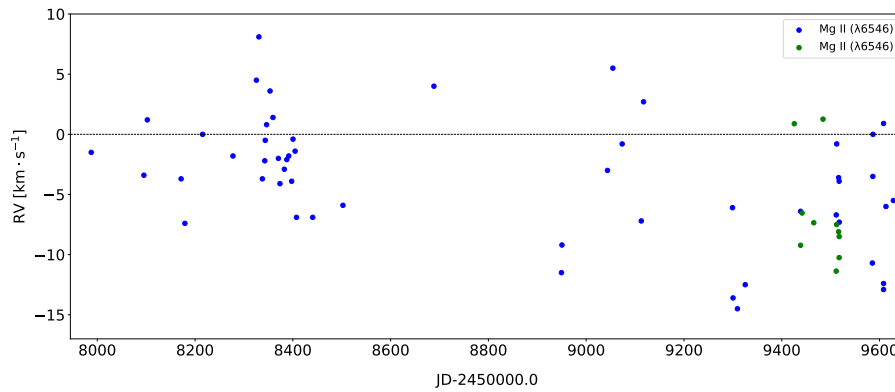


Figure 3.11: Measured radial velocities of magnesium line Mg II ($\lambda 6546$) - D700. Blue dots represent data from D700 and green ones are data from OES.

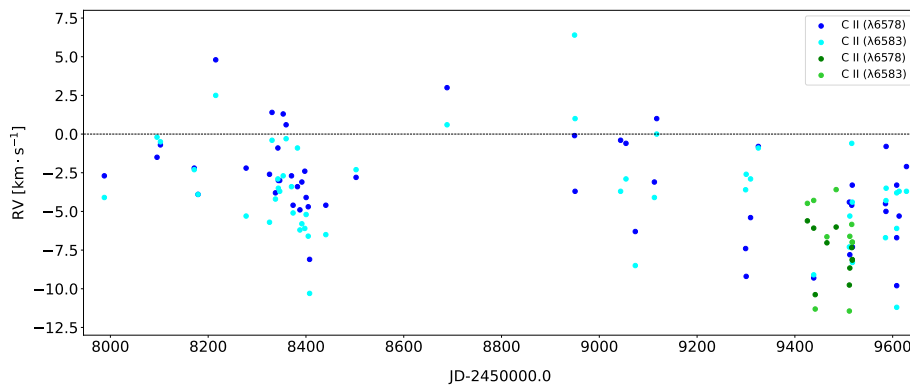


Figure 3.12: Measured radial velocities of two carbon lines C II ($\lambda 6578, 6583$) - D700. Blue dots represent data from D700 and green ones are data from OES.

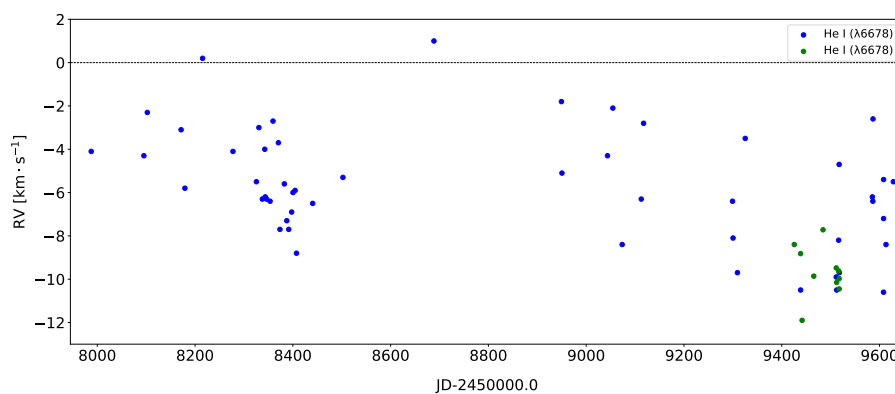


Figure 3.13: Measured radial velocities of helium line He I ($\lambda 6678$) - D700. Blue dots represent data from D700 and green ones are data from OES.

In many cases my analysis point to the existence of a transitional layer between layers with Si II and Fe II, and layers containing Mg II and C II, where the behavior is reversed

(contraction and expansion). Radial velocities of Fe II and Si II are negative, while those for C II lines, Mg II show positive values. For example on 2019 Jul 24 Si II lines are not pointing to contraction or expansion ($0.0 \text{ km} \cdot \text{s}^{-1}$) but Fe II together with H α have negative values of radial velocities, while radial velocities of C II lines, Mg II line and He I line are positive.

C II ($\lambda 6578, 6583$) and Mg II ($\lambda 6546$) (in Fig. 3.12 and Fig. 3.11) more often show positive values, which point to contraction in these concrete layers, but their pattern is different.

3.6.2 Data from ASP-32

Unfortunately, spectra from the Tartu observatory do not contain measurable DIB lines (presented ones reveal significant variability in profile), therefore the verification of stability hasn't been done. The accuracy of this spectrograph is similar to D700 but if we consider the fact that ASP-32 is moving together with the telescope, it will be probably higher and uncertainties resulting from the measurement are about $0.6 \text{ km} \cdot \text{s}^{-1}$. 2021 Nov 8 radial velocities of both Si II, Fe II and H α lines show high positive values (Tab. 3.4). It is assigned with a rapid contraction phase. Such an error could be caused by the fact that the spectrograph ASP-32 moves together with the telescope, but it would be considered in case when all lines are blue-shifted or red-shifted together. While only Mg II reached the minimum value $-18.3 \text{ km} \cdot \text{s}^{-1}$, other lines underwent their red-shifted maximum. Moreover, the value of radial velocity estimated for the Mg II line is consistent with the predicted period of about ± 400 days, so probably the rapid expansion of layers containing Fe II, Si II, and H α is real.

In Fig. 3.14 and Fig. 3.15 radial velocities of Si II and Fe II are plotted. Velocities copy similar curves while the average values are shifted. This is what has already been published by Abt 1957 for Si II and Fe II lines. Radial velocities of Si II ($\lambda 4028; 4030$) and Fe II (4508; 4515; 4520; 4522) revealed the same velocity curve shape but were shifted relative to each other.

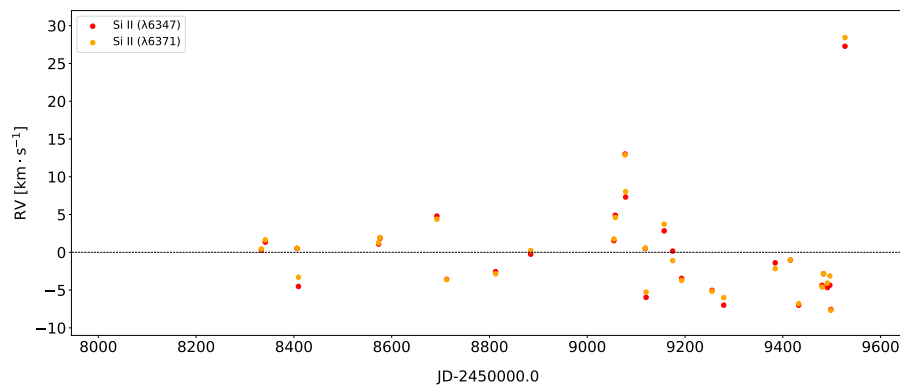


Figure 3.14: Measured radial velocities of two silicon lines Si II ($\lambda 6347, 6371$) - ASP-32.

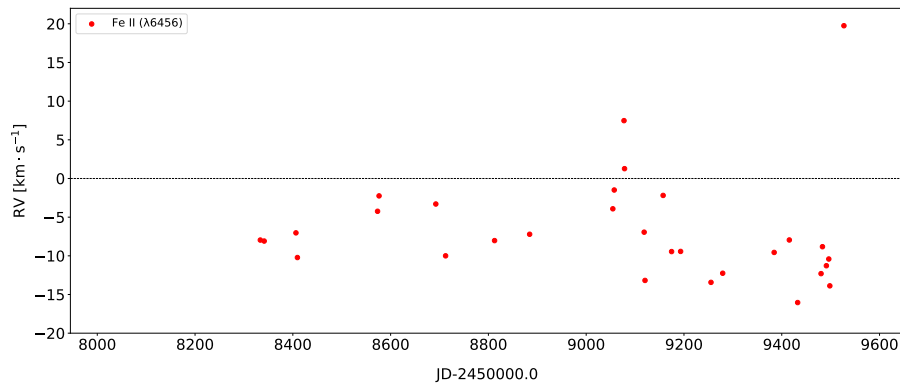


Figure 3.15: Measured radial velocities of iron line Fe II ($\lambda 6456$) - ASP-32.

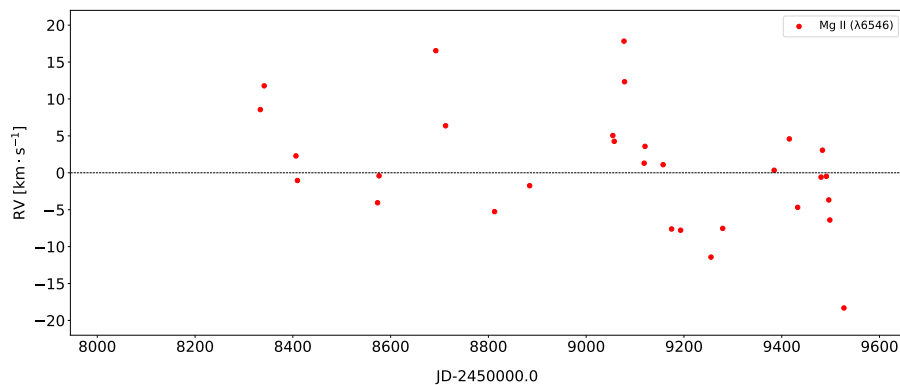


Figure 3.16: Measured radial velocities of magnesium line Mg II ($\lambda 6546$) - ASP-32.

3.6.3 OES Data

OES spectra cover just a fraction of the time. They were mainly used for comparison to data from D700 and ASP-32. Except for the Balmer lines and Na I D interstellar lines no additional line has been measured. In OES spectra DIB lines present highly asymmetric profiles, so for that reason, they were not used for verification of the stability of the spectrograph. Na I D interstellar lines were used instead. Radial velocities are plotted in Fig. 3.19 and based on this the estimated instability of OES is about $0.2 \text{ km} \cdot \text{s}^{-1}$. Usually to reach high accuracy the cross-correlation method by narrow lines is used, but in the case of this star which lines have their own behavior and vary on a time scale of hours, it is not considerable.

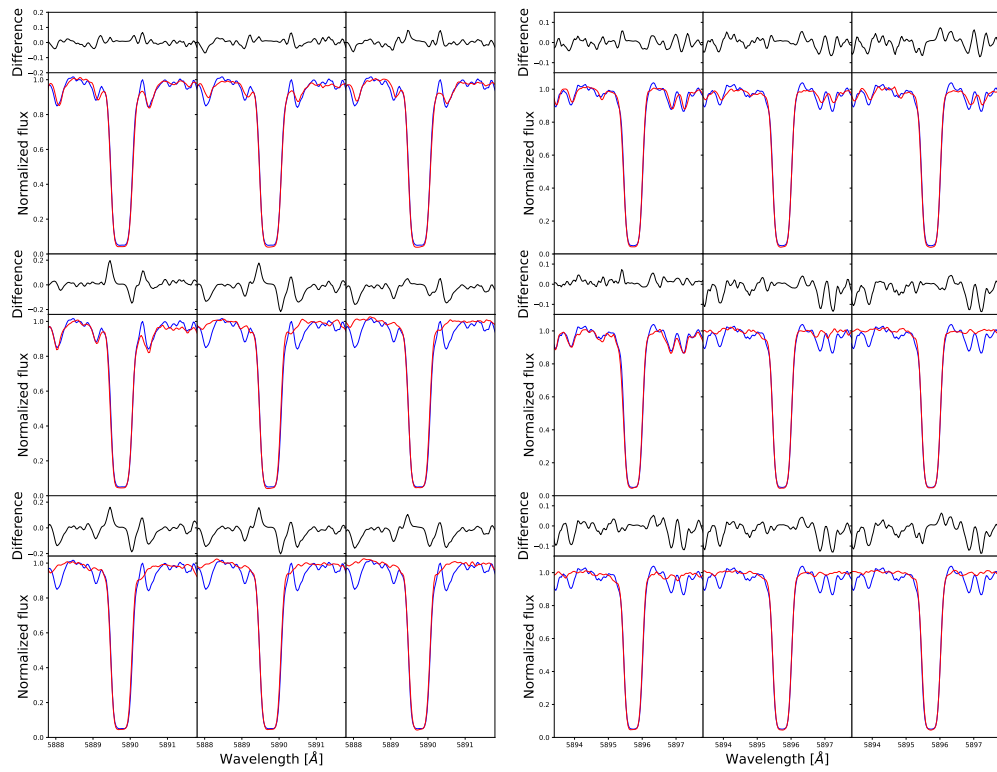
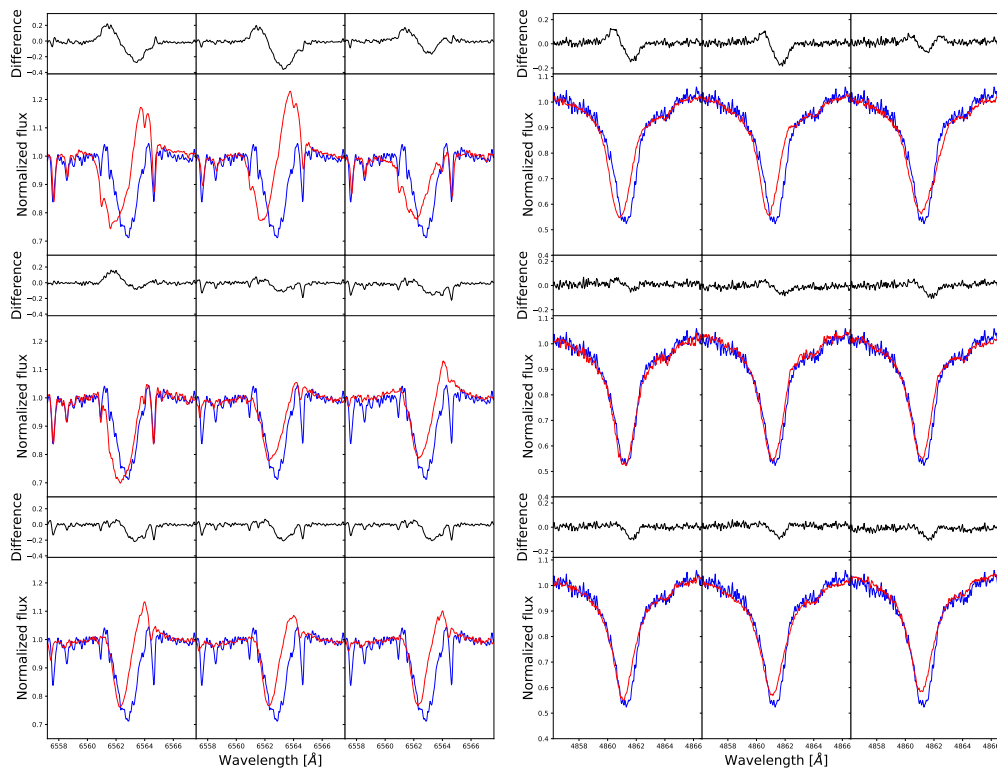
(a) Na I ($\lambda 5890$)(b) Na I ($\lambda 5896$)(c) H α ($\lambda 6563$)(d) H β ($\lambda 4861$)

Figure 3.17: Line profile variability of Na I D, H α and H β lines. The blue profile is a reference and the rest of the spectra compared to it are red. Their asymmetry is seen above (black line).

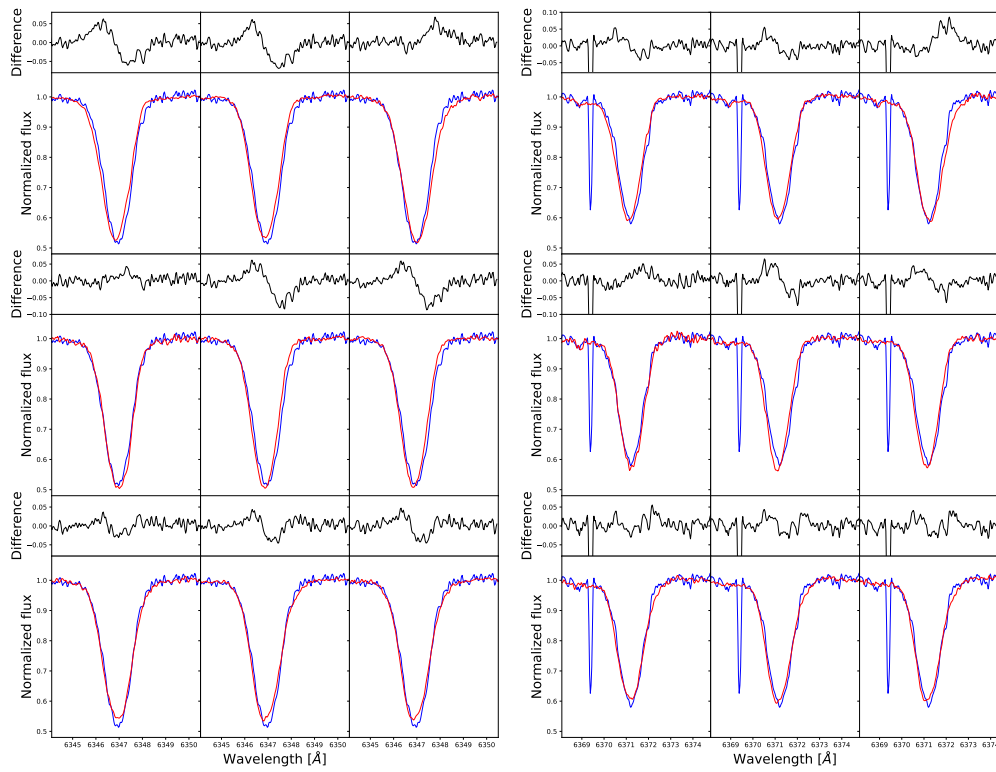
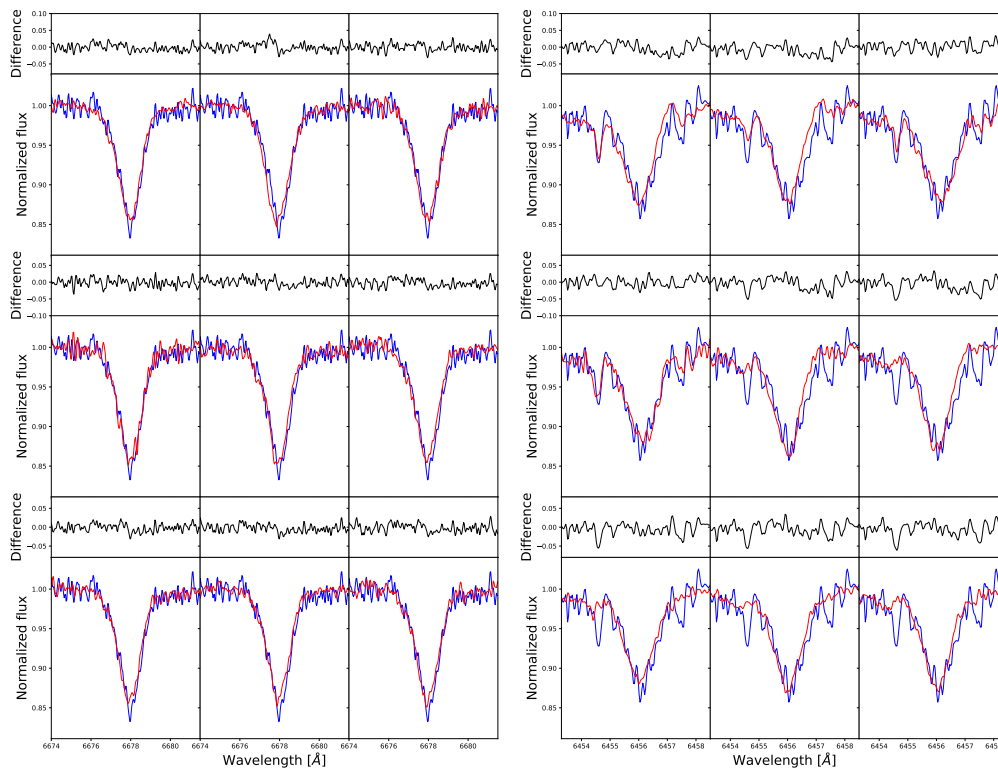
(a) Si II ($\lambda 6347$)(b) Si II ($\lambda 6371$)(c) He I ($\lambda 6678$)(d) Fe II $\lambda 6456$

Figure 3.18: Line profile variability of Si II, He I and Fe II lines. The blue profile is a reference and the rest of the spectra compared to it are red. Their asymmetry is seen above (black line).

The Fig. 3.18 (panel (a) and (b)) shows line profiles of Si II λ 6347;6371). It is composed of OES spectra where the first one (take on 2021 Jul 30) was used as reference one and the rest of them are compared to it. In Fig. 3.18 the first spectrum which is used as the standard one, another absorption line next to the Si II (λ 6371) appeared for the first time, no other spectra contain this absorption line. It is probably some artificial defect.

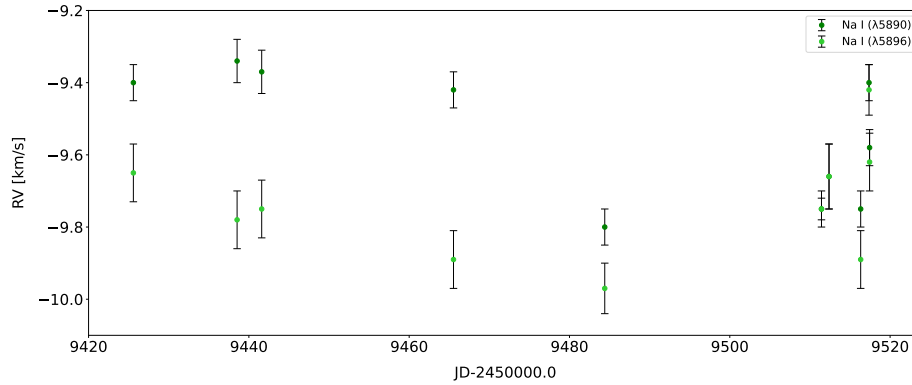


Figure 3.19: Measured radial velocities of sodium doublet Na I (λ 5890;5896) - OES. Estimated radial velocities were used to establish the stability of OES. All DIB lines were highly asymmetric so their measurement is inaccurate.

Spectra from OES have the largest wavelength coverage from examined data set, which allowed the investigation of other Balmer lines ($H\beta$, $H\gamma$, $H\delta$). $H\epsilon$ line is also included in the wavelength range, but its profile is the highly asymmetric and very close presence of Ca II (λ 3968) making the estimation of radial velocities more complicated (Fig. 3.3).

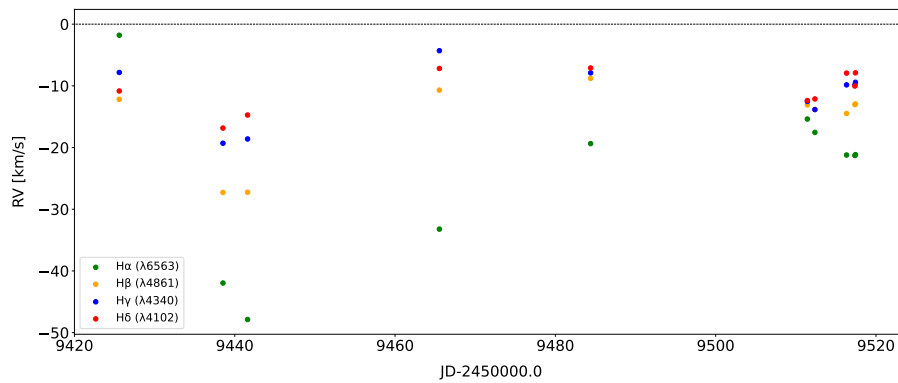


Figure 3.20: Measured radial velocities of Balmer lines $H\alpha$, $H\beta$, $H\gamma$, $H\delta$ (λ 6563;4861;4340;4102) - OES.

Fig. 3.20 present variability in radial velocities of measured Balmer lines, which is most significant for $H\alpha$. Normalization of $H\alpha$ region in the spectrum taken on 2021 Aug 12 went wrong, therefore the figures showing line profiles variability of Mg II, C II are not shown.

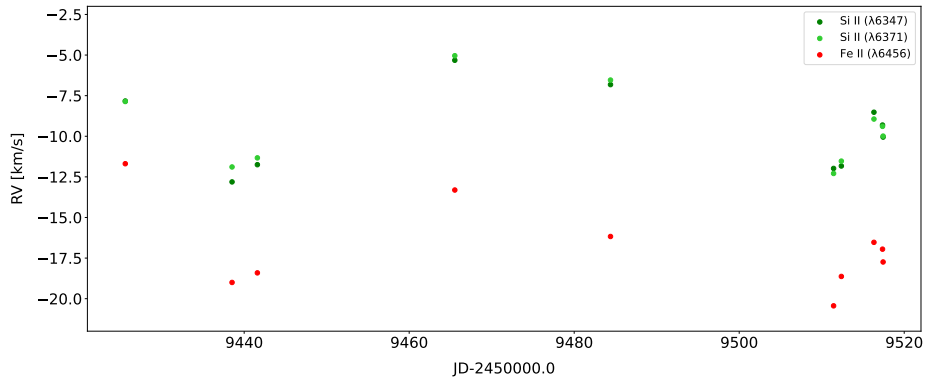


Figure 3.21: Measured radial velocities of iron Fe II ($\lambda 6456$) and silicon Si II ($\lambda 6347$; 6371) lines - OES.

Fig. 3.21 shows comparison of radial velocities of Fe II ($\lambda 6456$) and Si II ($\lambda 6347$; 6371) lines taken on shorter time scale by OES. As in Fig. 3.14 and Fig. 3.15, the radial velocities are shifted but follow the same shape. The displacement of Si II lines and Fe II lines on a shorter time scale, even considering of uncertainty given by the measurement, seems not to be constant. The same pattern may be seen in Fig. 3.9 and Fig. 3.10.

3.6.4 Short time changes

During the observational night on 2022 Jan 28 (Table 3.3) three spectra were taken. Radial velocities obtained at $17^{\text{h}}27^{\text{m}}13^{\text{s}}$ and $18^{\text{h}}17^{\text{m}}41^{\text{s}}$ UTC are very similar except Mg II line however the Mg II line and both C II lines at $18^{\text{h}}33^{\text{m}}17^{\text{s}}$ less than an hour later show the significantly higher negative value which is accompanied by the asymmetry in lines' profile. The line profile of $H\alpha$ is more asymmetric in the third spectrum than in the two previous.

On 2021 Oct 29 two OES spectra were obtained. In Fig. 3.18, Fig. 3.17 (two bottom right windows – taken during one observational night) almost no noticeable change is seen there. But in Tab. 3.5 the radial velocity of Mg II line differs about $\pm 2 \text{ km} \cdot \text{s}^{-1}$, and the changes are seen in the lines' profile. $H\alpha$ does not reveal dramatic changes in profile nor in radial velocities, however, one of the observed Balmer's lines does. Radial velocities of $H\delta$ as in the Mg II line differ about $\pm 2 \text{ km} \cdot \text{s}^{-1}$.

Table 3.3: Radial velocities of selected lines (in km/s) – D700.

Date UTC	Si II		Fe II		Mg II		H α core		C II		He I	
	λ 6347	λ 6371	λ 6456	λ 6545	λ 6563	λ 6578	λ 6582	λ 6678				
2017 Aug 22	-2.8	-3.3	-6.9	-1.5	-7.9	-2.7	-4.1	-4.1				
2017 Dec 7	-5.7	-5.2	-10.9	-3.4	-18.2	-1.5	-0.2	-4.3				
2017 Dec 14	-0.8	-1.1	-5.9	1.2	-14.3	-0.7	-0.5	-2.3				
2018 Feb 21	-4.8	-4.6	-9.4	-3.7	1.9	-2.2	-2.3	-3.1				
2018 Mar 1	-9.5	-8.9	-14.1	-7.4	-7.9	-3.9	-3.9	-5.8				
2018 Apr 6	-2.1	-1.2	-1.4	0.0	-9.3	4.8	2.5	0.2				
2018 Jun 8	-6.7	-6.1	-12.2	-1.8	-22.1	-2.2	-5.3	-4.1				
2018 Jul 25	-4.6	-4.4	-10.3	4.5	-51.1	-2.6	-5.7	-5.5				
2018 Jul 31	-0.2	-0.2	-4.6	8.1	-49.3	1.4	-0.4	-3.0				
2018 Aug 7	-5.4	-5.9	-11.6	-3.7	-51.5	-3.8	-4.2	-6.3				
2018 Aug 12	-5.0	-5.0	-9.6	-2.2	-54.6	-0.9	-2.9	-4.0				
2018 Aug 13	-6.5	-6.2	-11.2	-0.5	-54.5	-3.0	-3.5	-6.2				
2018 Aug 15	-9.0	-8.2	-14.1	0.8	-60.9	-3.0	-3.7	-6.3				
2018 Aug 22	-4.5	-4.1	-8.9	3.6	-19.0	1.3	-2.7	-6.4				
2018 Aug 28	-3.2	-2.7	-8.1	1.4	-54.9	0.6	-0.3	-2.7				
2018 Sep 8	-4.3	-4.6	-10.2	-2.0	-26.1	-2.7	-3.4	-3.7				
2018 Sep 12	-9.5	-9.5	-14.4	-4.1	-29.3	-4.6	-5.1	-7.7				
2018 Sep 21	-7.2	-6.6	-11.9	-2.9	-36.5	-3.4	-0.9	-5.6				
2018 Sep 26	-5.3	-4.7	-7.9	-2.1	-61.0	-4.9	-6.2	-7.3				
2018 Sep 30	-3.8	-3.4	-8.8	-1.8	-57.0	-3.1	-5.8	-7.7				
2018 Oct 6	-4.9	-4.4	-9.3	-3.9	-35.7	-2.4	-6.1	-6.9				
2018 Oct 8	-4.1	-4.5	-8.7	-0.4	-25.4	-4.1	-5.2	-6.0				
2018 Oct 13	-3.5	-3.6	-9.5	-1.4	-20.0	-4.7	-6.6	-5.9				
2018 Oct 15	-9.0	-9.1	-15.4	-6.9	-17.7	-8.1	-10.3	-8.8				
2018 Nov 18	-7.5	-7.7	-14.2	-6.9	-25.6	-4.6	-6.5	-6.5				

Table 3.3 – Continued

Date UTC	Si II	Si II	Fe II	Mg II	H α core	C II	C II	He I
2019 Jan 18	-5.9	-5.4	-11.9	-5.9	-17.2	-2.8	-2.3	-5.3
2019 Jul 24	0.0	0.0	-3.3	4.0	-56.6	3.0	0.6	1.0
2020 Apr 9	-5.0	-5.0	-8.9	-11.5	-16.5	-0.1	6.4	-1.8
2020 Apr 10	-6.3	-6.1	-10.9	-9.2	-19.0	-3.7	1.0	-5.1
2020 Jul 13	-7.0	-7.3	-13.8	-3.0	-36.8	-0.4	-3.7	-4.3
2020 Jul 24	-2.3	-2.3	-6.7	5.5	-34.0	-0.6	-2.9	-2.1
2020 Aug 12	-8.2	-7.8	-13.1	-0.8	-30.1	-6.3	-8.5	-8.4
2020 Sep 20	-9.6	-9.3	-13.9	-7.2	-17.5	-3.1	-4.1	-6.3
2020 Sep 24	-3.6	-4.2	-9.4	2.7	-25.9	1.0	0.0	-2.8
2021 Mar 25	-6.7	-6.7	-10.9	-6.1	-25.3	-7.4	-3.6	-6.4
2021 Mar 26	-7.9	-7.8	-12.9	-13.6	-26.1	-9.2	-2.6	-8.1
2021 Apr 4	-9.6	-9.4	-15.1	-14.5	-17.6	-5.4	-2.9	-9.7
2021 Apr 20	-5.7	-5.6	-13.7	-12.5	-29.1	-0.8	-0.9	-3.5
2021 Aug 12	-12.9	-11.8	-18.1	-6.4	-41.3	-9.3	-9.1	-10.5
2021 Oct 23	-8.8	-9.4	-16.3	-6.7	-14.8	-4.4	-7.3	-9.9
2021 Oct 24	-10.9	-10.8	-16.9	-0.8	-15.5	-7.8	-5.3	-10.5
2021 Oct 28	-4.0	-4.3	-13.2	-3.6	-18.2	-4.6	-0.6	-8.2
2021 Oct 29	-6.3	-6.3	-14.4	-3.9	-17.6	-3.3	-4.4	-4.7
2021 Oct 30	-9.8	-9.8	-16.6	-7.3	-22.5	-7.3	-8.3	-9.7
2022 Jan 5	-6.1	-7.6	-10.3	-10.7	-5.7	-4.5	-6.7	-6.2
2022 Jan 6	-5.9	-5.9	-9.6	-3.5	-5.9	-5.0	-4.3	-6.4
2022 Jan 7	-2.3	-2.4	-2.9	0.0	-5.8	-0.8	-3.5	-2.6
2022 Jan 28	-11.4	-11.5	-16.3	-12.9	-13.6	-6.7	-6.1	-10.6
2022 Jan 28	-7.5	-7.5	-12.5	-12.4	-8.9	-3.3	-3.8	-7.2
2022 Jan 28	-6.9	-9.4	-12.6	0.9	-7.2	-9.8	-11.2	-5.4
2022 Feb 2	-7.4	-7.1	-11.7	-6.0	-2.9	-5.3	-3.7	-8.4
2022 Feb 17	-6.2	-5.8	-8.0	-5.5	-10.8	-2.1	-3.7	-5.5

Table 3.3 – Continued

Date UTC	Si II	Si II	Fe II	Mg II	H α core	C II	C II	He I
Mean	-6.0	-6.0	-11.0	-3.6	-26.0	-3.3	-3.7	-5.7
Max. Value	0.0	0.0	-1.4	8.1	1.9	4.8	6.4	1.0
Min. Value	-12.9	-11.8	-18.1	-14.5	-61.0	-9.8	-11.2	-10.6

Table 3.4: Radial velocities of selected lines (in km/s) – ASP-32.

Date UTC	Si II	Si II	Fe II	Mg II	H α core
	λ 6347	λ 6371	λ 6456	λ 6545	λ 6563
2018 Aug 2	0.3	0.4	-8.0	8.6	-55.0
2018 Aug 10	1.4	1.7	-8.0	11.8	-55.6
2018 Oct 14	0.5	0.6	-7.0	2.3	-14.7
2018 Oct 17	-4.5	-3.3	-10.2	-1.0	-15.8
2019 Mar 30	1.1	1.3	-4.2	-4.1	-35.1
2019 Apr 2	1.9	2.0	-2.3	-0.4	-29.6
2019 Jul 27	4.8	4.4	-3.3	16.5	9.2
2019 Aug 16	-3.6	-3.6	-10.0	6.4	-22.0
2019 Nov 25	-2.6	-2.9	-8.0	-5.3	16.5
2020 Feb 4	-0.3	0.2	-7.2	-1.8	4.4
2020 Jul 24	1.5	1.8	-3.9	5.1	-32.4
2020 Jul 26	4.9	4.6	-1.5	4.3	-21.6
2020 Aug 15	13.0	12.9	7.5	17.8	-34.2
2020 Aug 16	7.3	8.0	1.3	12.3	-39.7
2020 Sep 26	0.5	0.6	-6.9	1.3	-19.6
2020 Sep 27	-6.0	-5.3	-13.2	3.6	-23.9
2020 Nov 3	2.8	3.7	-2.12	1.1	-19.2
2020 Nov 21	0.2	-1.1	-9.5	-7.6	30.6
2020 Dec 9	-3.5	-3.7	-9.4	-7.8	-12.5
2021 Feb 9	-5.0	-5.2	-13.4	-11.4	-7.3
2021 Mar 5	-7.0	-6.0	-12.3	-7.5	-29.3
2021 Jun 18	-1.4	-2.2	-9.6	0.3	29.5
2021 Jul 20	-1.0	-1.0	-8.0	4.6	-3.5
2021 Aug 6	-7.0	-6.8	-16.0	-4.7	-6.7
2021 Sep 22	-4.4	-4.6	-12.3	-0.6	-23.1
2021 Sep 25	-2.8	-2.9	-8.8	3.1	-20.3
2021 Oct 3	-4.7	-4.0	-11.3	-0.5	-11.9
2021 Oct 8	-4.4	-3.1	-10.4	-3.7	-17.8
2021 Oct 10	-7.6	-7.7	-13.9	-6.4	-16.9
2021 Nov 8	27.3	28.4	19.8	-18.3	28.8
Mean	0.0	0.2	-6.1	0.6	-15.0
Max. Value	27.3	28.4	38.5	17.8	30.6
Min. Value	-7.6	-7.7	-16.0	-18.3	-55.6

Table 3.5: Radial velocities of selected lines (in km/s) – OES.

Date UTC	H δ	H γ	H β	Na I	Na I	Si II	Si II
	λ 4102	λ 4340	λ 4861	λ 5890	λ 5896	λ 6347	λ 6371
2021 Jul 30	-10.8	-7.8	-12.2	-9.4	-9.7	-7.8	-7.9
2021 Aug 12	-16.8	-19.3	-27.3	-9.3	-9.8	-12.8	-11.9
2021 Aug 15	-14.7	-18.6	-27.2	-9.4	-9.8	-11.8	-11.3
2021 Sep 8	-7.2	-4.3	-10.7	-9.4	-9.9	-5.3	-5.0
2021 Sep 26	-7.1	-7.9	-8.8	-9.8	-10.0	-6.8	-6.5
2021 Oct 23	-12.4	-12.5	-13.1	-9.8	-9.8	-12.0	-12.3
2021 Oct 24	-12.1	-13.8	-13.8	-9.7	-9.7	-11.8	-11.5
2021 Oct 28	-7.9	-9.8	-14.5	-9.8	-9.9	-8.5	-8.9
2021 Oct 29	-10.0	-9.8	-13.0	-9.4	-9.4	-9.3	-9.4
2021 Oct 29	-7.9	-9.4	-12.9	-9.6	-9.6	-10.1	-10.0
Mean value	-10.7	-11.3	-15.4	-9.5	-9.7	-9.6	-9.5
Max. value	-7.1	-4.3	-8.8	-9.3	-9.4	-5.3	-5.0
Min. value	-16.8	-19.3	-27.3	-9.8	-10.0	-12.8	-12.3
Date UTC	Fe II	Mg II	H α	C II	C II	He I	
	λ 6456	λ 6545	λ 6563	λ 6578	λ 6582	λ 6678	
2021 Jul 30	-11.7	0.9	-1.8	-5.6	-4.5	-8.4	
2021 Aug 12	-19.0	-9.2	-42.0	-6.1	-4.3	-8.8	
2021 Aug 15	-18.4	-6.5	-47.9	-10.4	-11.3	-11.9	
2021 Sep 8	-13.3	-7.4	-33.2	-7.0	-6.6	-9.9	
2021 Sep 26	-16.2	1.3	-19.4	-6.0	-3.6	-7.7	
2021 Oct 23	-20.4	-11.4	-15.4	-9.8	-11.4	-9.5	
2021 Oct 24	-18.6	-7.5	-17.5	-8.7	-6.6	-10.2	
2021 Oct 28	-16.5	-8.1	-21.2	-7.3	-5.8	-9.6	
2021 Oct 29	-17.0	-10.3	-21.3	-8.1	-7.0	-10.0	
2021 Oct 29	-17.7	-8.5	-21.2	-8.2	-7.7	-10.5	
Mean value	-16.9	-6.7	-24.1	-7.7	-6.8	-9.6	
Max. value	-11.7	1.3	-1.8	-5.6	-3.6	-7.7	
Min. value	-20.4	-11.4	-47.9	-10.4	-11.4	-11.9	

Conclusion

This thesis aims to summarize the information about A-type supergiant HD 21389 from studies that have been published previously and expand this knowledge for new findings coming out from my analysis of five years of spectroscopic observation in the optical region.

Collected information about HD 21389 is outlined in the first chapter with regards to its membership in a group of variable stars which is named after α Cyg as α Cyg variables.

For analysis performed in this study 92 spectra of HD 21389 in the optical region were reduced using IRAF and IDL-based package with some additional correction steps (telluric correction, barycentric velocity correction, and DIBs correction for spectra taken by spectrograph D700) which were done out of IRAF.

It is known that some kind of long-term variability may be observed in stellar spectra of supergiant stars, whether it is in line profile, radial velocities, or even the appearance of new spectral lines. According to my results, the spectrum of HD 21389 in addition to long-term changes (longer than a month) also displays the rapid (several hours or days) variability in lines' profiles and radial velocities. The most striking changes are recorded for $H\alpha$ line and its closest surrounding. However this is based only on five examples, the extended wings around $H\alpha$ that we detected for the first time vary in strength, where the trend of variability shows correlation with the shape of the central line profile, which reflects conditions in its atmosphere. Also, my analysis revealed a High-Velocity Absorption event which HD 21389 underwent during July-August 2018.

All other lines present variability in lines' profile, and except the Na I D also in radial velocities. Appearance and disappearance of asymmetry in lines' profile reflect the actual condition of $H\alpha$ line which is associated with active and quiescent phases of its atmosphere.

Future Insights

One of the future insights is to verify whether this star has a 7.7 day-long period observable in iron (Fe II) lines, which was reported by Abt [1957](#).

Periodic behavior in radial velocities of the Mg II line has been observed in data from Tartu Observatory, and also data obtained by the D700 spectrograph suggest the presence of a cycle with a period close to one year. Unfortunately, the data set taken by ASP-32 show mainly positive values, while the spectra from Ondřejov rather present negative values. Together they form periodic structures, but their comparability is questionable and therefore we are already planning observations taken by OES.

Although the extended wings presented in spectra of O- and B-type supergiants especially around the $H\alpha$ line have been observed and discussed several decades ago (e.g.

Ebbets 1980, 1982), nature of their variability noticed in spectra of HD 21389 as A-type supergiant (whether it is real) is still in the plane of suggestions. The first step would be to confirm our results with a larger amount of spectra, thus proving the dependency between the strength of the wings and the central line profile. If this is would be confirmed, then an effort will be made to find the physical causes of such changes.

Bibliography

- [1] (accessed September 20, 2021). *Perek 2-m Telescope*. <http://stelweb.asu.cas.cz/en/telescope/>.
- [2] (accessed September 20, 2021). *Echelle Spectrograph*. <https://stelweb.asu.cas.cz/en/telescope/instrumentation/oes-spectrograph/>.
- [3] (accessed September 20, 2021). *SIMBAD*. <http://simbad.u-strasbg.fr/simbad/sim-basic?Ident=HD+21389&submit=SIMBAD+search>.
- [4] (accessed April 17, 2022). *Geneva database*. <https://www.unige.ch/sciences/astro/evolution/en/database/syclist/>.
- [5] (accessed November 7, 2021). *AZT-12*. <https://kosmos.ut.ee/en/services/telescopes>.
- [6] (accessed November 11, 2021). *ASP-12*. <https://sirius.to.ee/aret/1.5m.html>.
- [7] (accessed Mars 18, 2022). *Single Order Spectrograph*. <https://stelweb.asu.cas.cz/~slechta/2mEN/single/>.
- [8] (accessed November 30, 2021). *Elodie*. <http://atlas.obs-hp.fr/elodie/>.
- [9] (accessed November 30, 2021). *Perek 2-m*. <https://stelweb.asu.cas.cz/~slechta/2m/>.
- Abt, Helmut A. (July 1957). “The Variability of Supergiants.” In: *ApJ* 126, p. 138. DOI: [10.1086/146379](https://doi.org/10.1086/146379).
- Achmad, L., H. J. G. L. M. Lamers, and L. Pasquini (Apr. 1997). “Radiation driven wind models for A, F and G supergiants.” In: *A&A* 320, pp. 196–208.
- Adelman, S., A. Gulliver, and B. Smalley (Jan. 2003). “Round Table on Instrumentation and Data Processing”. In:
- Aydin, C. (July 1972). “Atmospheres of A-type supergiants.” In: *A&A* 19, p. 369.
- Bailer-Jones, C. A. L., J. Rybizki, M. Fouesneau, M. Demleitner, et al. (Mar. 2021). “Estimating Distances from Parallaxes. V. Geometric and Photogeometric Distances to 1.47 Billion Stars in Gaia Early Data Release 3”. In: *AJ* 161.3, 147, p. 147. DOI: [10.3847/1538-3881/abd806](https://doi.org/10.3847/1538-3881/abd806). arXiv: [2012.05220](https://arxiv.org/abs/2012.05220) [[astro-ph.SR](#)].
- Bailer-Jones, C. A. L., J. Rybizki, M. Fouesneau, G. Mantelet, et al. (Aug. 2018). “Estimating Distance from Parallaxes. IV. Distances to 1.33 Billion Stars in Gaia Data Release 2”. In: *AJ* 156.2, 58, p. 58. DOI: [10.3847/1538-3881/aacb21](https://doi.org/10.3847/1538-3881/aacb21). arXiv: [1804.10121](https://arxiv.org/abs/1804.10121) [[astro-ph.SR](#)].
- Barlow, M. J. and M. Cohen (May 1977). “Infrared photometry and mass loss rates for OBA supergiants and Of stars.” In: *ApJ* 213, pp. 737–755. DOI: [10.1086/155204](https://doi.org/10.1086/155204).
- Campbell, William Wallace et al. (Jan. 1911). “Sixty-eight stars whose radial velocities vary”. In: *Lick Observatory Bulletin* 199, pp. 140–154. DOI: [10.5479/ADS/bib/1911LicOB.6.140C](https://doi.org/10.5479/ADS/bib/1911LicOB.6.140C).

- Catelan, M. and H. A. Smith (2015). *Pulsating Stars*.
- Corliss, David J., Nancy D. Morrison, and Saul J. Adelman (Dec. 2015). “Spectroscopic and Photometric Variability in the A0 Supergiant HR 1040”. In: *AJ* 150.6, 190, p. 190. DOI: [10.1088/0004-6256/150/6/190](https://doi.org/10.1088/0004-6256/150/6/190).
- de Jager, C. (1984). *The brightest stars*.
- de Jager, C., H. Nieuwenhuijzen, and K. A. van der Hucht (Feb. 1988). “Mass loss rates in the Hertzsprung-Russell diagram.” In: *A&AS* 72, pp. 259–289.
- Denizman, L. and M. Hack (Oct. 1988). “Spectra and radial velocities of white supergiants.” In: *A&AS* 75, pp. 79–92.
- Ducati, J. R. (Jan. 2002). “VizieR Online Data Catalog: Catalogue of Stellar Photometry in Johnson’s 11-color system.” In: *VizieR Online Data Catalog*.
- Ebbets, D. (Jan. 1980). “The variable H- α P CYG profile of α Cam : 09.5 Ia.” In: *ApJ* 235, pp. 97–103. DOI: [10.1086/157614](https://doi.org/10.1086/157614).
- (Apr. 1982). “The structure and variability of H α emission in early-type supergiants.” In: *ApJS* 48, pp. 399–414. DOI: [10.1086/190783](https://doi.org/10.1086/190783).
- Ekström, S. et al. (Jan. 2012). “Grids of stellar models with rotation. I. Models from 0.8 to 120 M_{\odot} at solar metallicity ($Z = 0.014$ ”). In: *A&A* 537, A146, A146. DOI: [10.1051/0004-6361/201117751](https://doi.org/10.1051/0004-6361/201117751). arXiv: [1110.5049](https://arxiv.org/abs/1110.5049) [[astro-ph.SR](#)].
- Fath, Edward Arthur (Jan. 1935). “Pulsation in stellar atmospheres ; Atmospheric extinction at Mt. Hamilton”. In: *Lick Observatory Bulletin* 474, pp. 115–121. DOI: [10.5479/ADS/bib/1935LicOB.17.115F](https://doi.org/10.5479/ADS/bib/1935LicOB.17.115F).
- Friedman, Scott D. et al. (Jan. 2011). “Studies of Diffuse Interstellar Bands V. Pairwise Correlations of Eight Strong DIBs and Neutral Hydrogen, Molecular Hydrogen, and Color Excess”. In: *ApJ* 727.1, 33, p. 33. DOI: [10.1088/0004-637X/727/1/33](https://doi.org/10.1088/0004-637X/727/1/33). arXiv: [1011.2951](https://arxiv.org/abs/1011.2951) [[astro-ph.GA](#)].
- Gaia Collaboration (Nov. 2020). “VizieR Online Data Catalog: Gaia EDR3 (Gaia Collaboration, 2020)”. In: *VizieR Online Data Catalog*, I/350, pp. I/350.
- Gautschi, A. (Apr. 2009). “Deneb’s variability: a hint of a deep-lying convection zone?” In: *A&A* 498.1, pp. 273–279. DOI: [10.1051/0004-6361/200911666](https://doi.org/10.1051/0004-6361/200911666).
- Georgy, C., H. Saio, and G. Meynet (Mar. 2014). “The puzzle of the CNO abundances of α Cygni variables resolved by the Ledoux criterion.” In: *MNRAS* 439, pp. L6–L10. DOI: [10.1093/mnrasl/slt165](https://doi.org/10.1093/mnrasl/slt165). arXiv: [1311.4744](https://arxiv.org/abs/1311.4744) [[astro-ph.SR](#)].
- Gray, R. O. and R. F. Garrison (Dec. 1987). “The Early A-Type Stars: Refined MK Classification, Confrontation with Stroemgren Photometry, and the Effects of Rotation”. In: *ApJS* 65, p. 581. DOI: [10.1086/191237](https://doi.org/10.1086/191237).
- Israelian, G., E. Chentsov, and F. Musaev (Sept. 1997). “The inhomogeneous circumstellar envelope of Rigel (beta Orionis A)”. In: *MNRAS* 290.3, pp. 521–532. DOI: [10.1093/mnras/290.3.521](https://doi.org/10.1093/mnras/290.3.521).
- Kabáth, P. et al. (Jan. 2020). “Ondrejov Echelle Spectrograph, Ground Based Support Facility for Exoplanet Missions”. In: *Publications of the Astronomical Society of the Pacific* 132.1009, p. 035002. DOI: [10.1088/1538-3873/ab6752](https://doi.org/10.1088/1538-3873/ab6752). URL: <https://doi.org/10.1088/1538-3873/ab6752>.
- Karzas, W. J. and R. Latter (May 1961). “Electron Radiative Transitions in a Coulomb Field.” In: *ApJS* 6, p. 167. DOI: [10.1086/190063](https://doi.org/10.1086/190063).

- Kasai, Eli (Apr. 2013). "THE TYPE IA SUPERNOVA RATE IN INTERMEDIATE RED-SHIFT GALAXY CLUSTERS". PhD thesis. DOI: [10.13140/RG.2.1.2808.8803](https://doi.org/10.13140/RG.2.1.2808.8803).
- Kaufer, A., O. Stahl, B. Wolf, T. Gaeng, C. A. Gummertsbach, I. Jankovics, et al. (Oct. 1996). "Long-term spectroscopic monitoring of BA-type supergiants. II. High-velocity absorptions in β Ori and HD96919." In: *A&A* 314, pp. 599–608.
- Kaufer, A., O. Stahl, B. Wolf, T. Gaeng, C. A. Gummertsbach, J. Kovacs, et al. (Jan. 1996). "Long-term spectroscopic monitoring of BA-type supergiants. I. H_{α} -line-profile variability." In: *A&A* 305, p. 887.
- Koubsky, P. et al. (Jan. 2004). "Ondrejov Echelle Spectrograph - OES". In: *Publications of the Astronomical Institute of the Czechoslovak Academy of Sciences*.
- Kraus, M. et al. (Sept. 2015). "Interplay between pulsations and mass loss in the blue supergiant 55 Cygnus = HD 198 478". In: *A&A* 581, A75, A75. DOI: [10.1051/0004-6361/201425383](https://doi.org/10.1051/0004-6361/201425383). arXiv: [1507.01846](https://arxiv.org/abs/1507.01846) [[astro-ph.SR](#)].
- Kudritzki, R. P. et al. (Oct. 1999). "The wind momentum-luminosity relationship of galactic A- and B-supergiants". In: *A&A* 350, pp. 970–984. arXiv: [astro-ph/9910449](https://arxiv.org/abs/astro-ph/9910449) [[astro-ph](#)].
- Kunasz, P. B., N. D. Morrison, and B. Spessart (Mar. 1983). "Mass loss in HR 1040 (AO Ia) : analysis of MG I Λ 2802 and $H\alpha$." In: *ApJ* 266, pp. 739–746. DOI: [10.1086/160820](https://doi.org/10.1086/160820).
- Lallement, R. et al. (Apr. 1993). "Correction of spectra for telluric absorption lines with the help of a molecular data bank and high resolution forward modelling: H₂O lines around the sodium doublet at 589.5 NM". In: *A&A* 271, p. 734.
- Lefever, K., J. Puls, and C. Aerts (Mar. 2007). "Statistical properties of a sample of periodically variable B-type supergiants. Evidence for opacity-driven gravity-mode oscillations". In: *A&A* 463.3, pp. 1093–1109. DOI: [10.1051/0004-6361:20066038](https://doi.org/10.1051/0004-6361:20066038). arXiv: [astro-ph/0611484](https://arxiv.org/abs/astro-ph/0611484) [[astro-ph](#)].
- Lucy, L. B. (June 1976). "An analysis of the variable radial velocity of Alpha Cygni." In: *ApJ* 206, pp. 499–508. DOI: [10.1086/154405](https://doi.org/10.1086/154405).
- Lyder, David A. (Nov. 2001). "The Stars in Camelopardalis OB1: Their Distance and Evolutionary History". In: *AJ* 122.5, pp. 2634–2643. DOI: [10.1086/323705](https://doi.org/10.1086/323705).
- Maharramov, Y. M. and A. Sh. Baloglanov (Jan. 2015). "Spectroscopic Variability of the Supergiants HD21389 and HD187982". In: *Odessa Astronomical Publications* 28, p. 39.
- Markova, N. et al. (Aug. 2008). "Wind structure of late B supergiants. I. Multi-line analyses of near-surface and wind structure in HD 199 478 (B8 Iae)". In: *A&A* 487.1, pp. 211–221. DOI: [10.1051/0004-6361:200809376](https://doi.org/10.1051/0004-6361:200809376). arXiv: [0806.0929](https://arxiv.org/abs/0806.0929) [[astro-ph](#)].
- McCarthy, James K. et al. (June 1997). "Mass-Loss Rates and Stellar Wind Momenta of A-Supergiants in M31: First Results from the Keck HIRES Spectrograph". In: *ApJ* 482.2, pp. 757–764. DOI: [10.1086/304189](https://doi.org/10.1086/304189).
- Morgan, W. W., A. E. Whitford, and A. D. Code (Sept. 1953). "Studies in Galactic Structure. I. a Preliminary Determination of the Space Distribution of the Blue Giants." In: *ApJ* 118, p. 318. DOI: [10.1086/145754](https://doi.org/10.1086/145754).
- Morrison, N. D., R. Rother, and N. Kurschat (Apr. 2008). " $H\alpha$ line profile variability in the B8Ia-type supergiant Rigel (β Ori)". In: *Clumping in Hot-Star Winds*. Ed. by Wolf-Rainer Hamann, Achim Feldmeier, and Lidia M. Oskinova, p. 155.

- Percy, J. R. and D. L. Welch (Aug. 1983). “Photometric variability of B- and A-type supergiants.” In: *Publications of the ASP* 95, pp. 491–505. DOI: [10.1086/131198](https://doi.org/10.1086/131198).
- Praderie, F., A. Talavera, and H. J. G. L. M. Lamers (June 1980). “Resonance line profiles in A type supergiants from IUE and Copernicus spectra.” In: *A&A* 86, pp. 271–282.
- Przybilla, N. et al. (July 2010). “Mixing of CNO-cycled matter in massive stars”. In: *A&A* 517, A38, A38. DOI: [10.1051/0004-6361/201014164](https://doi.org/10.1051/0004-6361/201014164). arXiv: [1005.2278](https://arxiv.org/abs/1005.2278) [[astro-ph.SR](https://arxiv.org/abs/1005.2278)].
- Richardson, N. D. et al. (Jan. 2011). “A Five-year Spectroscopic and Photometric Campaign on the Prototypical α Cygni Variable and A-type Supergiant Star Deneb”. In: *AJ* 141.1, 17, p. 17. DOI: [10.1088/0004-6256/141/1/17](https://doi.org/10.1088/0004-6256/141/1/17). arXiv: [1009.5994](https://arxiv.org/abs/1009.5994) [[astro-ph.SR](https://arxiv.org/abs/1009.5994)].
- Rosendhal, J. D. (Dec. 1973). “A survey of H-alpha emission in early-type high-luminosity stars.” In: *ApJ* 186, p. 909. DOI: [10.1086/152555](https://doi.org/10.1086/152555).
- Saad, S. M., M. A. Hamdy, and M. S. Abolazm (Dec. 2012). “An overview investigation of Be/Shell stars”. In: *NRIAG Journal of Astronomy and Geophysics* 1.2, pp. 97–105. DOI: [10.1016/j.nrjag.2012.12.004](https://doi.org/10.1016/j.nrjag.2012.12.004).
- Saio, H. et al. (Oct. 2006). “MOST Detects g- and p-Modes in the B Supergiant HD 163899 (B2 Ib/II)”. In: *ApJ* 650.2, pp. 1111–1118. DOI: [10.1086/507409](https://doi.org/10.1086/507409). arXiv: [astro-ph/0606712](https://arxiv.org/abs/astro-ph/0606712) [[astro-ph](https://arxiv.org/abs/astro-ph/0606712)].
- Saio, Hideyuki, Cyril Georgy, and Georges Meynet (Aug. 2013). “Evolution of blue supergiants and α Cygni variables: puzzling CNO surface abundances”. In: *MNRAS* 433.2, pp. 1246–1257. DOI: [10.1093/mnras/stt796](https://doi.org/10.1093/mnras/stt796). arXiv: [1305.2474](https://arxiv.org/abs/1305.2474) [[astro-ph.SR](https://arxiv.org/abs/1305.2474)].
- Schaller, G. et al. (Dec. 1992). “New Grids of Stellar Models from 0.8-SOLAR-MASS to 120-SOLAR-MASS at Z=0.020 and Z=0.001”. In: *A&AS* 96, p. 269.
- Skoda, Petr (Jan. 1996). “SPEFO—A Simple, Yet Powerful Program for One-Dimensional Spectra Processing”. In: *Astronomical Data Analysis Software and Systems V*. Ed. by George H. Jacoby and Jeannette Barnes. Vol. 101. Astronomical Society of the Pacific Conference Series, p. 187.
- Slechts, Miroslav and Petr Skoda (Jan. 2002). “2-meter telescope devices: coudé slit spectrograph and HEROS”. In: *Publications of the Astronomical Institute of the Czechoslovak Academy of Sciences* 90, pp. 1–4.
- Snow T. P., Jr. and D. C. Morton (Nov. 1976). “Copernicus ultraviolet observations of mass-loss effects in O and B stars.” In: *ApJS* 32, pp. 429–465. DOI: [10.1086/190404](https://doi.org/10.1086/190404).
- Straižys, V. and V. Laugalys (Jan. 2007). “Young Stars in the Camelopardalis Dust and Molecular Clouds. I. The Cam OB1 Association”. In: *Baltic Astronomy* 16, pp. 167–182. arXiv: [0803.2461](https://arxiv.org/abs/0803.2461) [[astro-ph](https://arxiv.org/abs/0803.2461)].
- (2008). “Young Stars and Clouds in Camelopardalis”. In: *Handbook of Star Forming Regions, Volume I*. Ed. by B. Reipurth. Vol. 4, p. 294.
- Takeda, Yoichi and Masahide Takada-Hidai (Feb. 2000). “Helium and Carbon Abundances in Late-B and Early-A Supergiants”. In: *Publications of the ASJ* 52, p. 113. DOI: [10.1093/pasj/52.1.113](https://doi.org/10.1093/pasj/52.1.113).
- Talavera, A. and A. I. Gomez de Castro (July 1987). “The UV high resolution spectrum of A-type supergiants.” In: *A&A* 181, pp. 300–314.
- Verdugo, E., A. Talavera, and A. I. Gómez de Castro (June 1999a). “Understanding A-type supergiants. I. Ultraviolet and visible spectral atlas”. In: *A&AS* 137, pp. 351–362. DOI: [10.1051/aas:1999487](https://doi.org/10.1051/aas:1999487).

- (June 1999b). “Understanding A-type supergiants. II. Atmospheric parameters and rotational velocities of Galactic A-type supergiants”. In: *A&A* 346, pp. 819–830.
- Wright, A. E. and M. J. Barlow (Jan. 1975). “The radio and infrared spectrum of early type stars undergoing mass loss.” In: *MNRAS* 170, pp. 41–51. DOI: [10.1093/mnras/170.1.41](https://doi.org/10.1093/mnras/170.1.41).
- Zeinalov, S. K. and A. Kh. Rzaev (Oct. 1990a). “Nonstationary Atmospheres of Supergiants - Part One - Systematic Movement of Matter in the Atmospheres of Stars HD21291 and HD21389”. In: *Astrophysics and Space Science* 172.2, pp. 211–216. DOI: [10.1007/BF00643311](https://doi.org/10.1007/BF00643311).
- (Oct. 1990b). “Nonstationary Atmospheres of Supergiants - Part Two - the H α Profile Variations in the Spectra of HD21291 and HD21389”. In: *Astrophysics and Space Science* 172.2, pp. 217–224. DOI: [10.1007/BF00643312](https://doi.org/10.1007/BF00643312).

Appendix

Here is example Python code to correct 1D spectra in fits format for barycentric velocity:

```
import numpy as np
from astropy.time import Time
from astropy.io import fits
from astropy.coordinates import SkyCoord, EarthLocation
from astropy import units as u
import glob
import os

path_to_file = '/home/...'
files = glob.glob(path_to_file + '*.fit')

def corr (file):
    spectrum = fits.open(file)
    latitude = spectrum[0].header['LATITUDE']
    longitude = spectrum[0].header['LONGITUD']
    altitude = spectrum[0].header['HEIGHT']
    ra = spectrum[0].header['RA']
    sep_ra = ra.split(':')
    r = (float(sep_ra[0]) + float(sep_ra[1])/60
        + float(sep_ra[2])/3600)*15
    dec = spectrum[0].header['DEC']
    sep_dec = dec.split(':')
    d = float(sep_dec[0]) + float(sep_dec[1])/60
        + float(sep_dec[2])/3600
    jd = spectrum[0].header['JDATE']
    '''
    date = spectrum[0].header['DATE-OBS']
    time = spectrum[0].header['UT']
    full_time = date + 'T' + time
    t = Time(full_time, scale = 'utc')
    julian_date = t.jd
    '''

    obs_location =
    EarthLocation.from_geodetic(lat = latitude*u.deg, lon =
                                longitude*u.deg, height =
                                altitude*u.m)

    object_coordinates = SkyCoord(ra = r*u.deg, dec = d*u.deg)

    barycentric_correction = object_coordinates.
                                radial_velocity_correction(
```

```

                                obstime = Time(jd, format = '
                                jd'), location = obs_location)

bc = barycentric_correction.to_value(u.km/u.s)

return bc#, julian_date

def wav (file):
    spec = fits.open(file)
    dw = spec[0].header['CDEL1']
    wave = np.ones(spec[0].header['NAXIS1'], dtype=float)
    for i in range (spec[0].header['NAXIS1']):
        wave[i] = spec[0].header['CRVAL1'] + i*spec[0].header['
                                CDEL1']

    return wave, dw

for i in list(files):
    c = 299792.458 #km/s
    barcor = corr(i)[0]
    #JD = corr(i)[1]
    wave_new = wav(i)[0]*(1+(barcor/c))
    dw_new = wav(i)[1]*(1+(barcor/c))
    fits.setval(i, 'CRVAL1', value = wave_new[0])
    fits.setval(i, 'CDEL1', value = dw_new)
    fits.setval(i, 'BARCOR', value = barcor)
    #fits.setval(i, 'JD', value = JD)

```

It provides barycentric velocity correction for all .fit/.fits files in the given folder, which is defined at the beginning. Function `corr (file)` takes .fit/.fits as an input. It extracts keywords from the header (latitude, longitude, height for the location of the observatory; the position of an object in RA and DEC coordinates - RA is converted from hour angle to angular degrees; additionally it can deal with julian date instead of time given in UTC). Using the `astropy` package it calculates the value of barycentric velocity.

Function `wav (file)` returns array of all wavelength points and the value of distance between each wavelength points ('CDEL1').

In the end, all files are opened, barycentric velocity is calculated separately for each file, it recalculates starting wavelength point and their distance according to

$$\lambda_{corrected} = \lambda_{old} \cdot \left(1 + \frac{v_{barycentric}}{c}\right)$$

And finally it is written to header, 'BARCOR' is the new keyword for value of barycentric velocity, 'CRVAL1' and 'CDEL1' are rewritten after they are corrected for velocity.

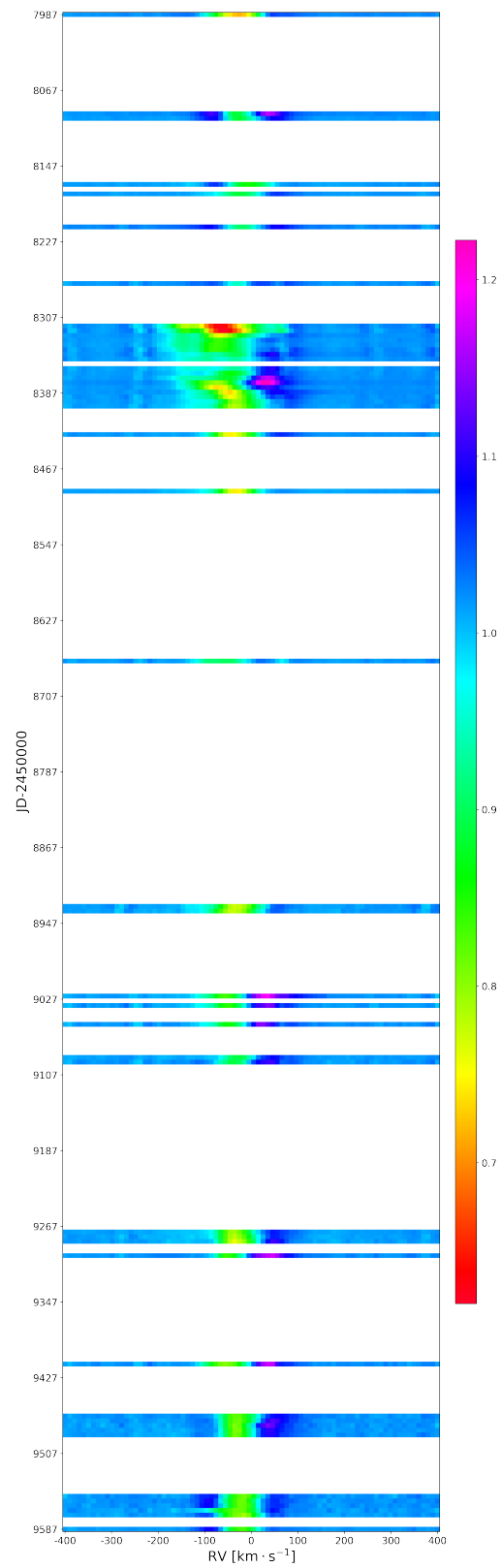


Figure 4.22: Dynamical spectrum of H α from D700. Color bar at the right side represents the flux.

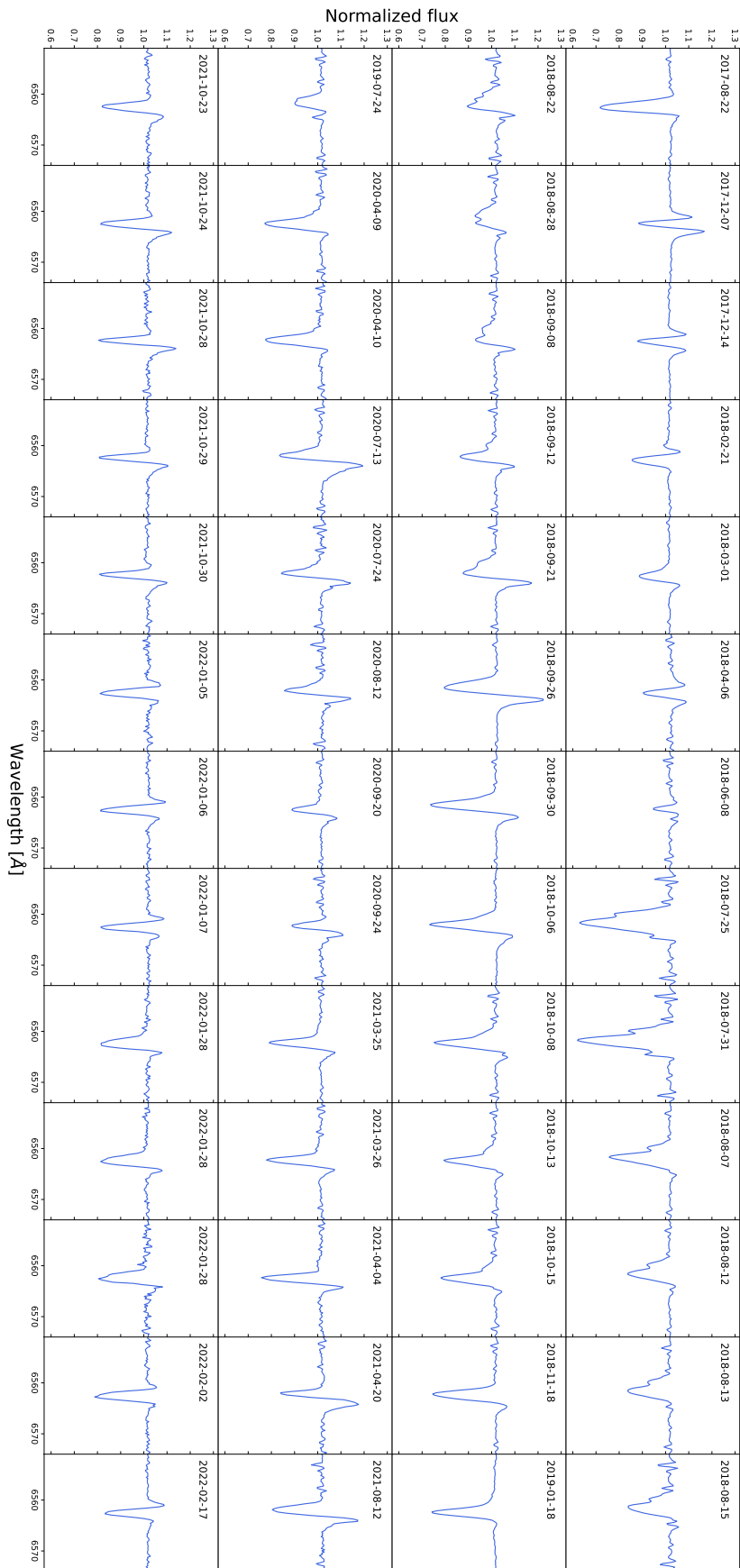
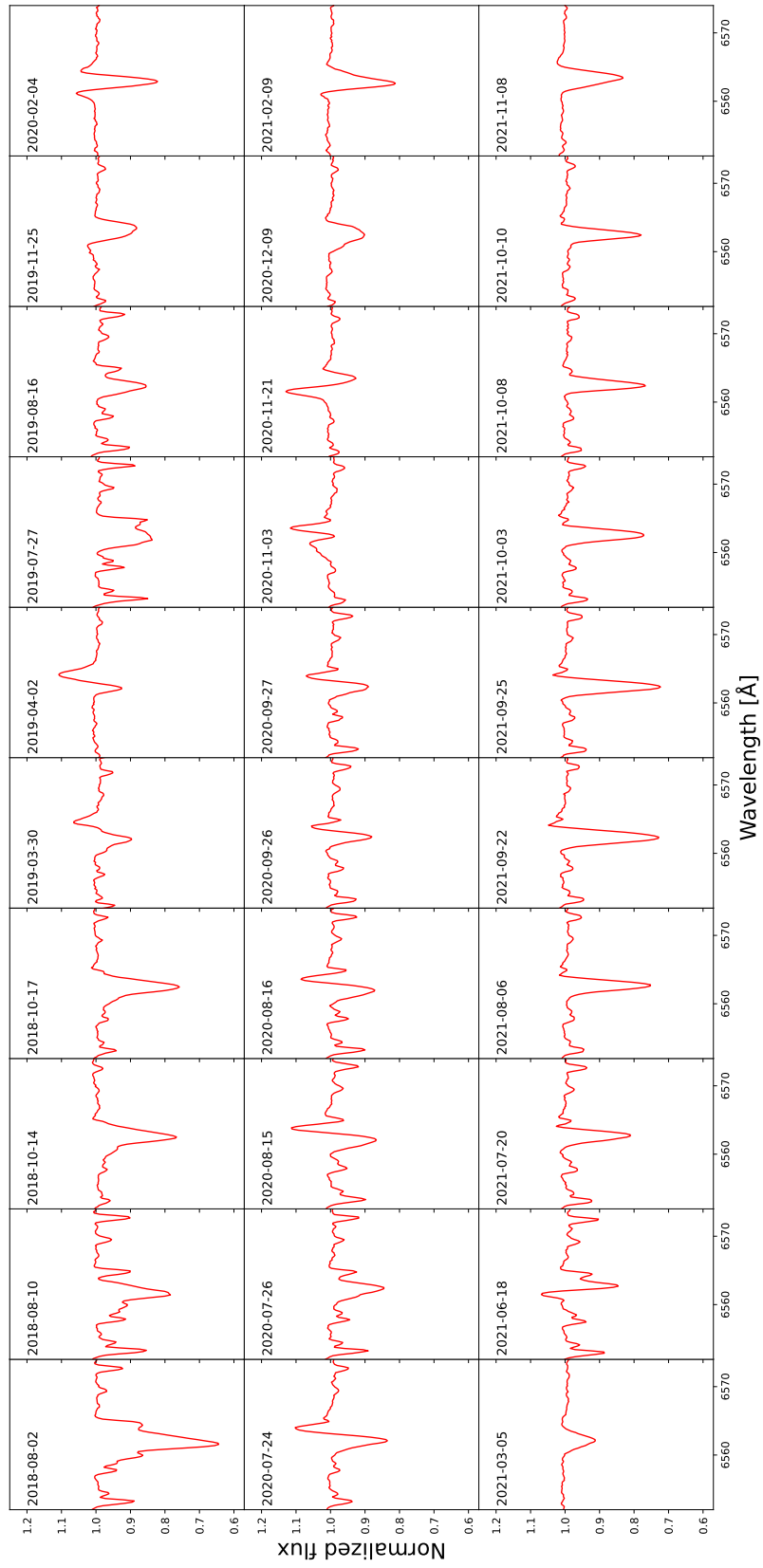


Figure 4.23: H α line profile variability (spectrograph D700).

Figure 4.24: H α line profile variability (ASP-32 spectrograph).

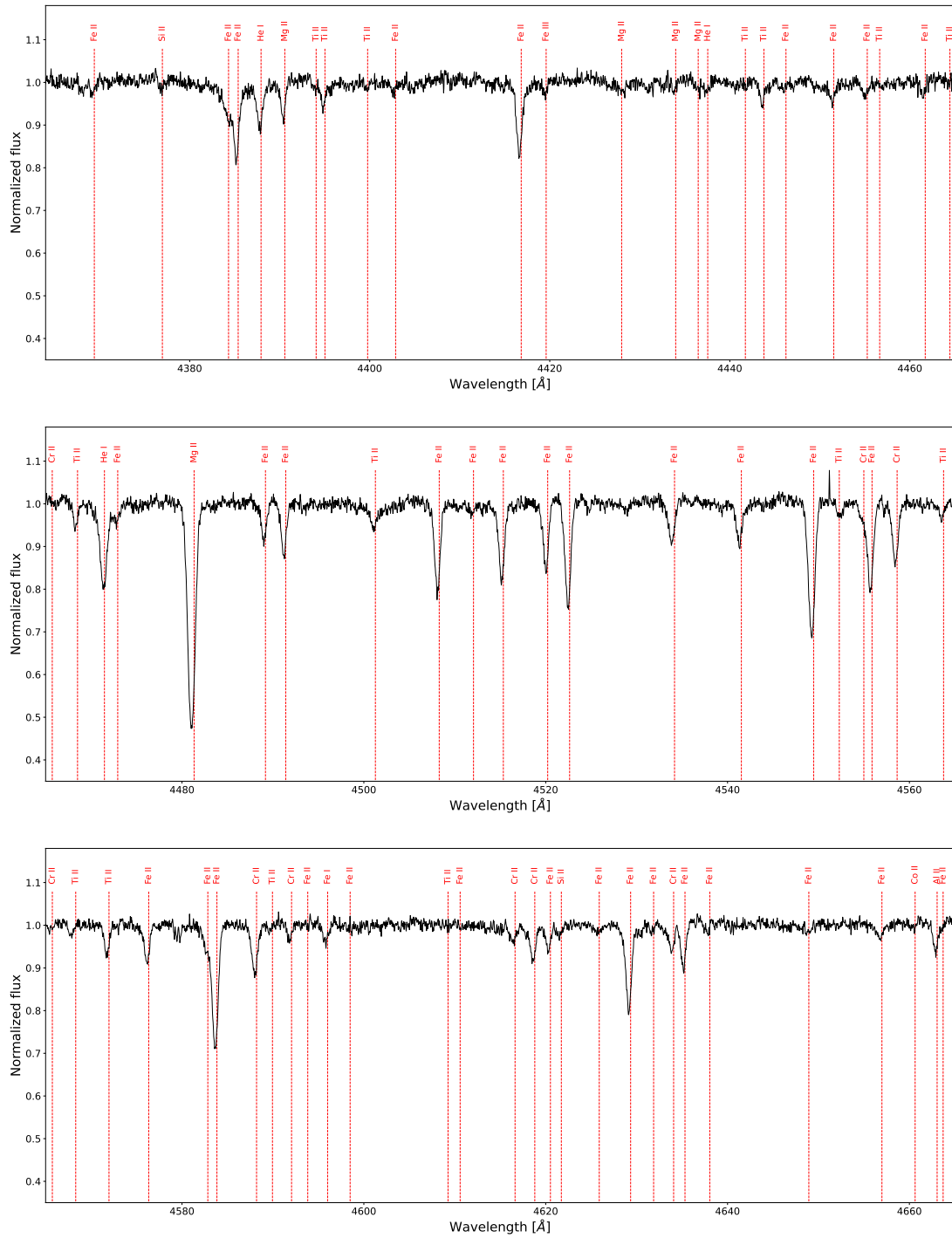


Figure 4.26: OES spectrum: identified spectral lines in region from $\sim 4360 \text{ \AA}$ to $\sim 4660 \text{ \AA}$.

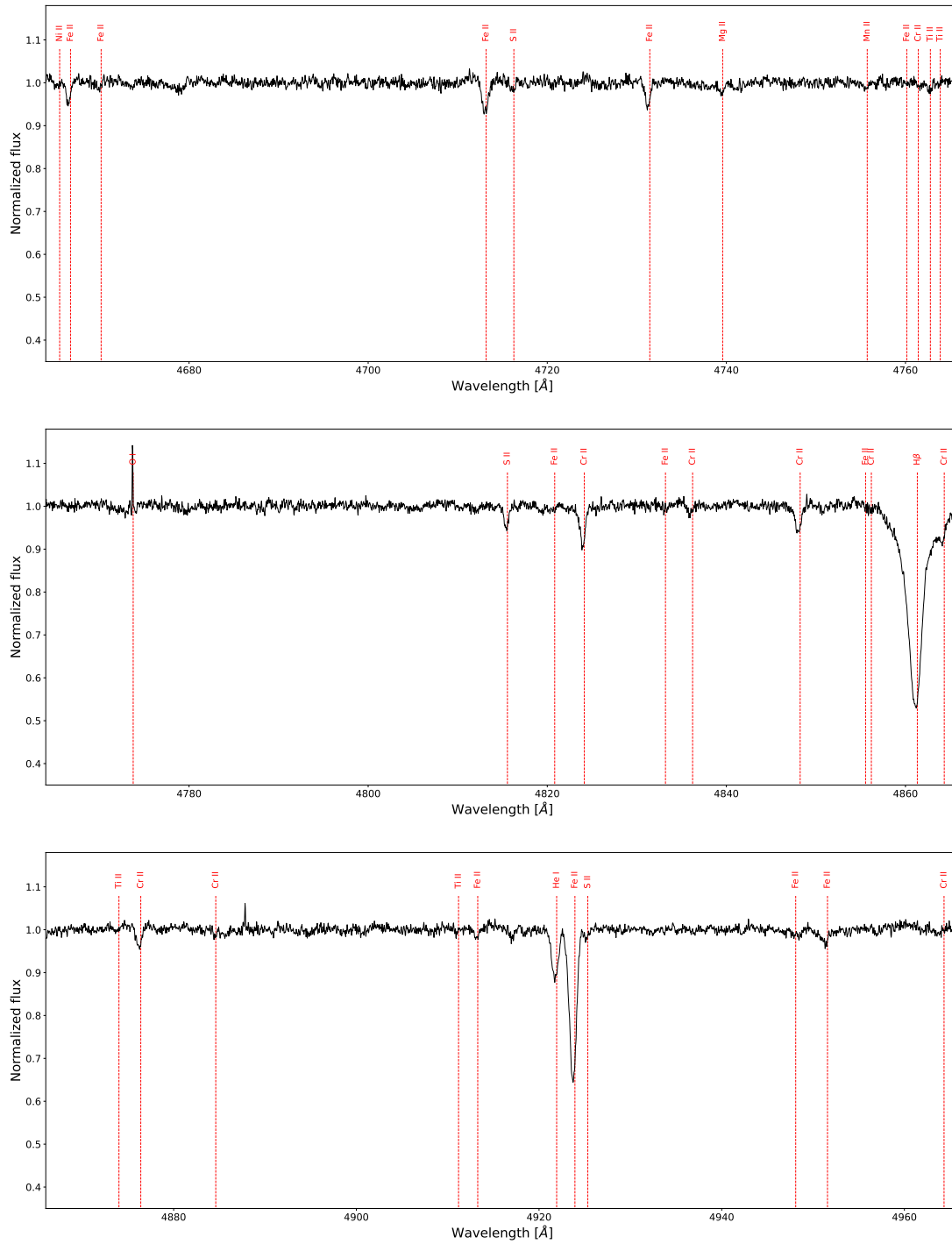


Figure 4.27: OES spectrum: identified spectral lines in region from ~ 4660 Å to ~ 4960 Å.

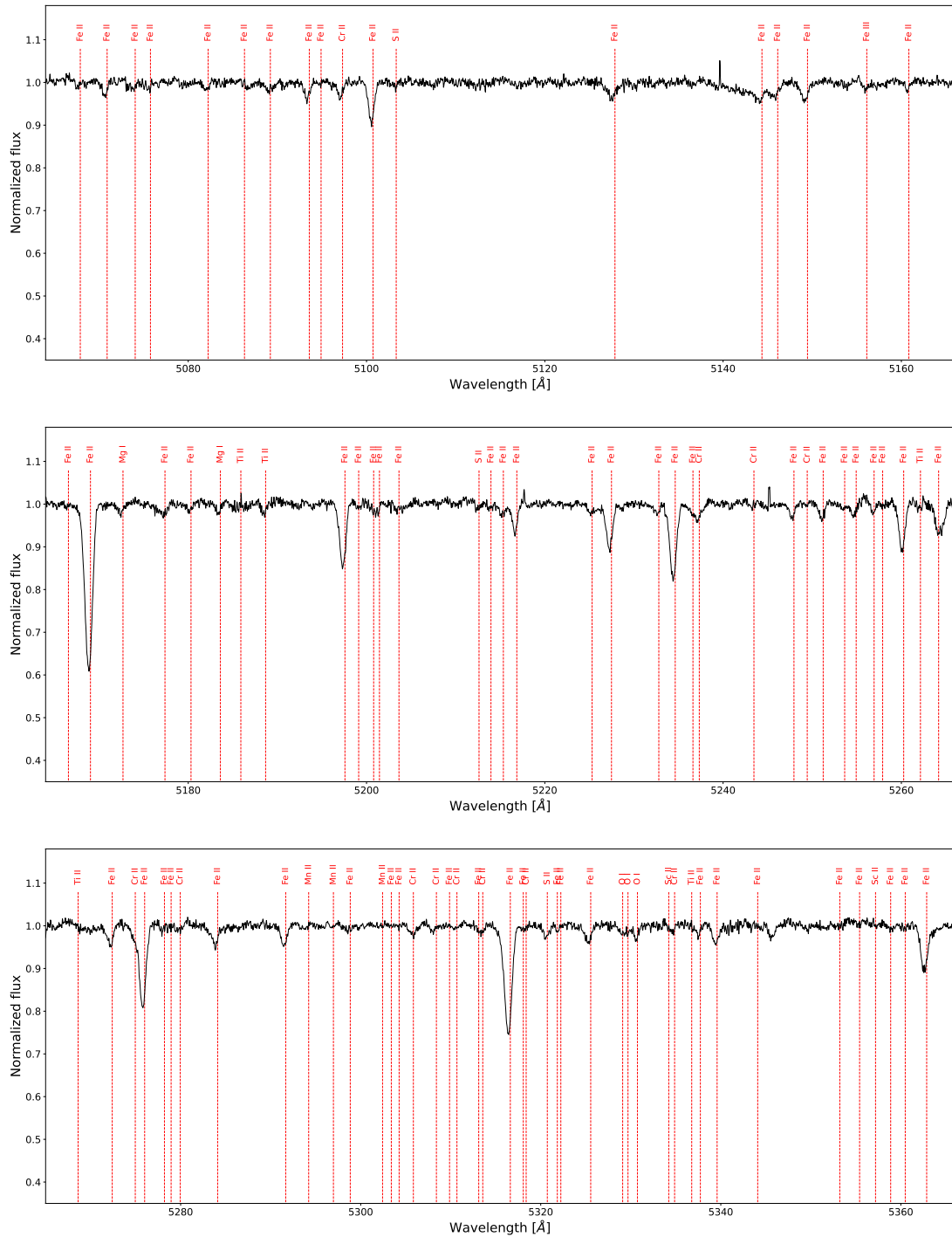


Figure 4.28: OES spectrum: identified spectral lines in region from $\sim 5060 \text{ \AA}$ to $\sim 5360 \text{ \AA}$.

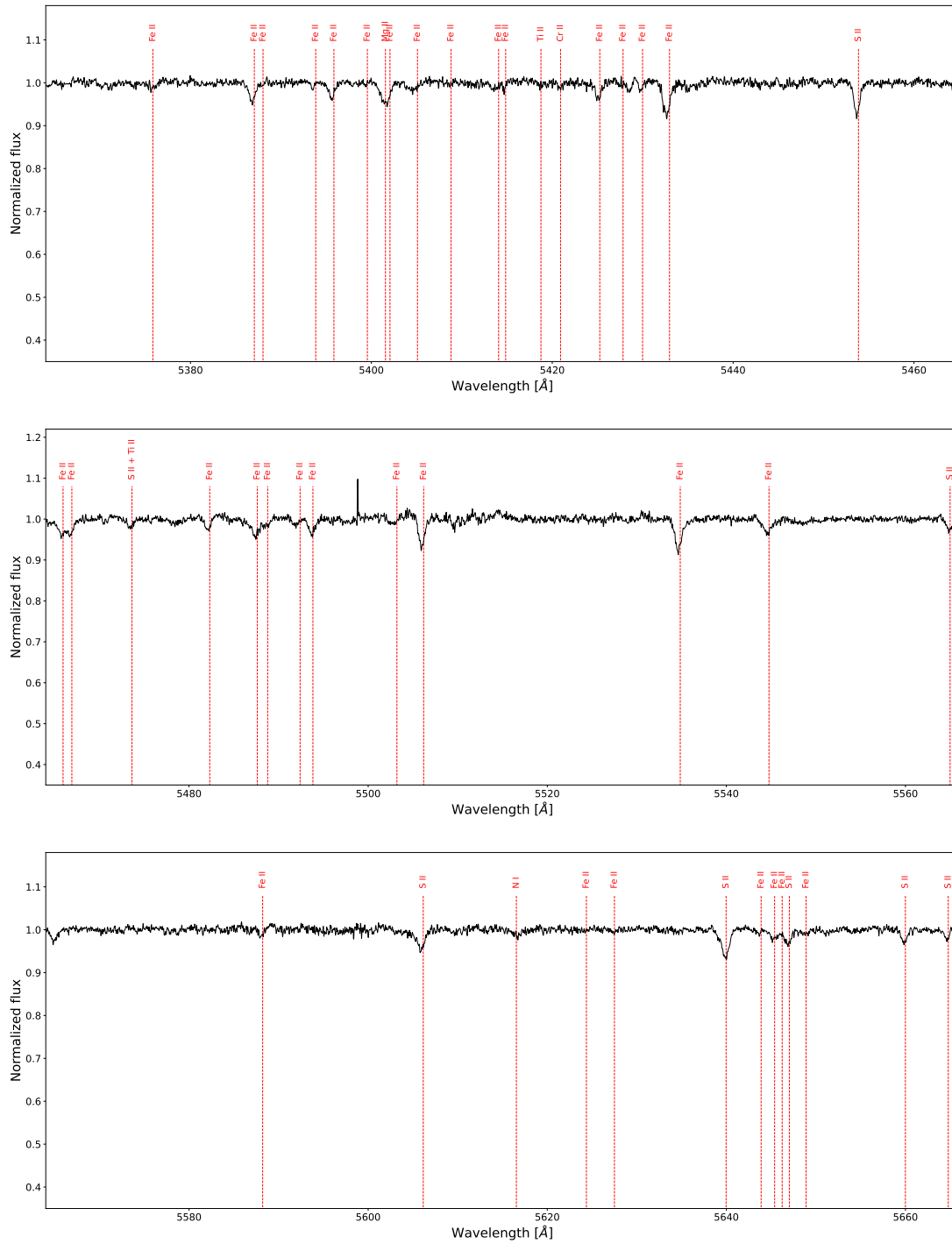


Figure 4.29: OES spectrum: identified spectral lines in region from $\sim 5360 \text{ \AA}$ to $\sim 5660 \text{ \AA}$.

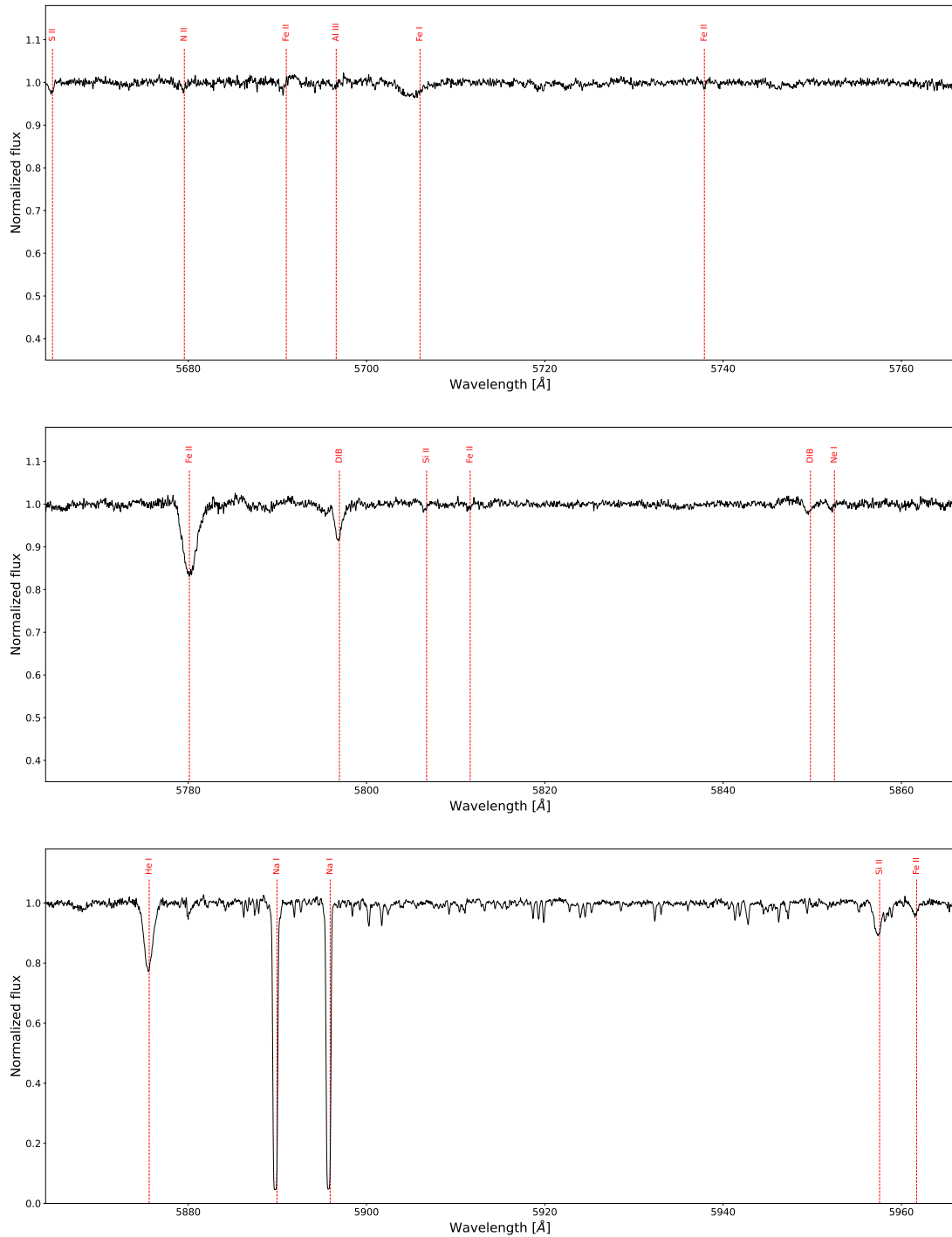


Figure 4.30: OES spectrum: identified spectral lines in region from $\sim 5660 \text{ \AA}$ to $\sim 5960 \text{ \AA}$.

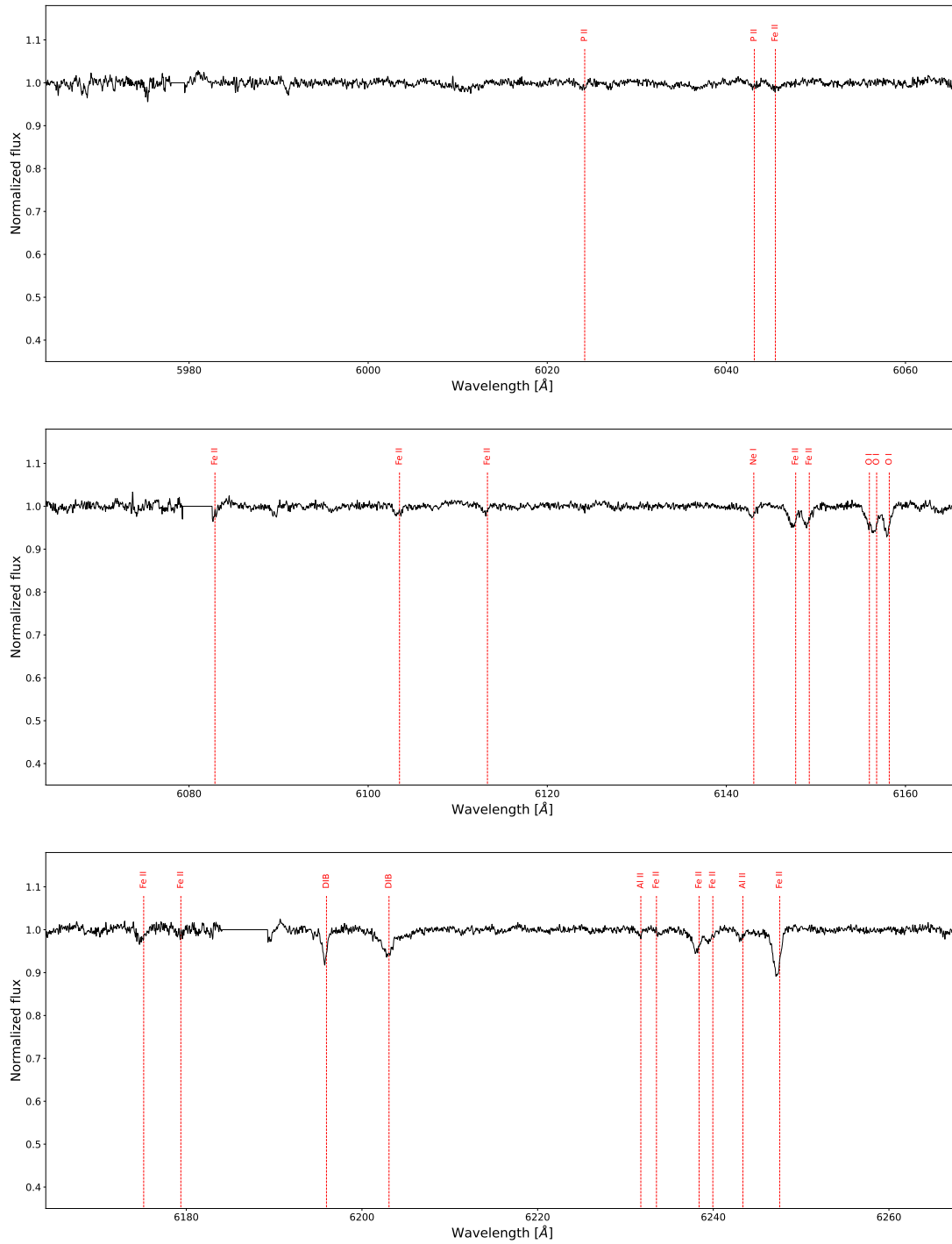


Figure 4.31: OES spectrum: identified spectral lines in region from $\sim 5960 \text{ \AA}$ to $\sim 6260 \text{ \AA}$.

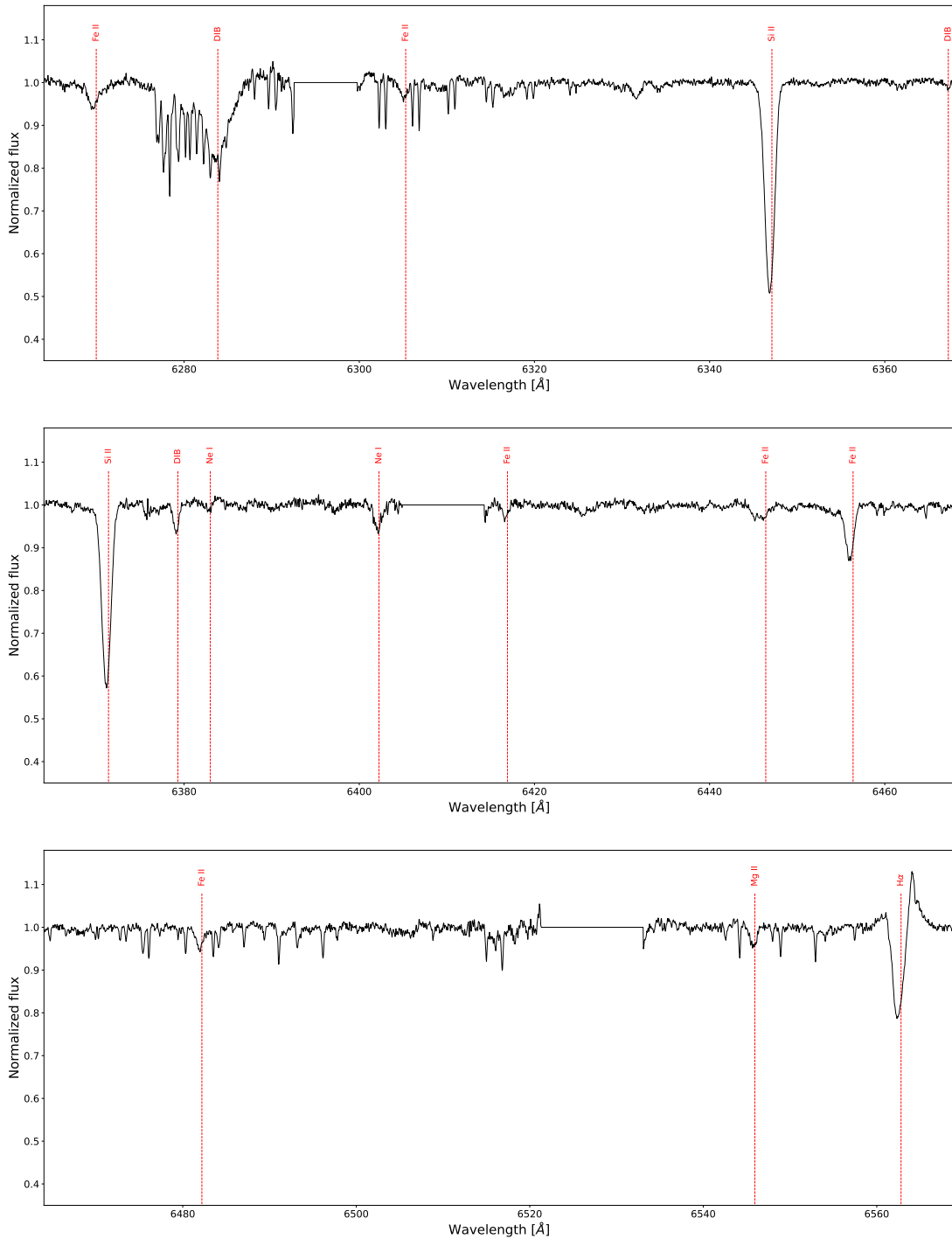


Figure 4.32: OES spectrum: identified spectral lines in region from $\sim 6260 \text{ \AA}$ to $\sim 6560 \text{ \AA}$.

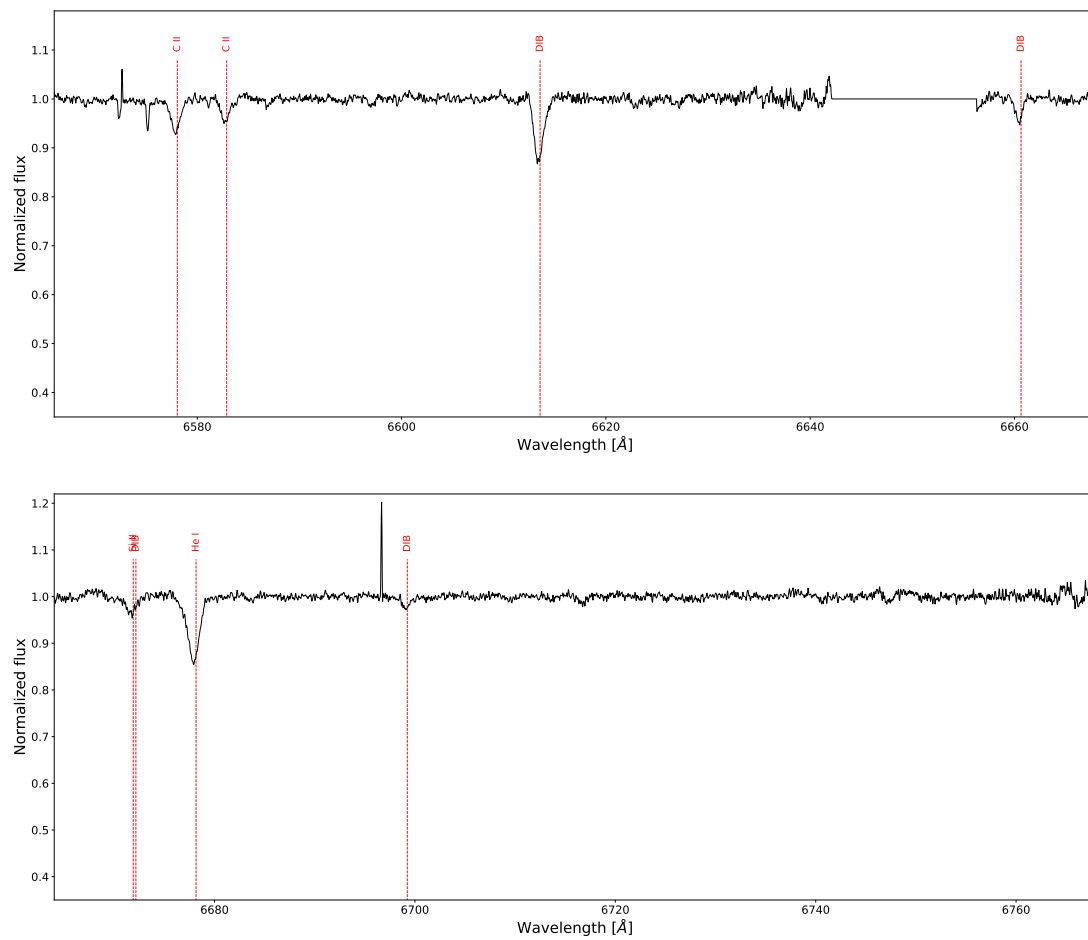


Figure 4.33: OES spectrum: identified spectral lines in region from $\sim 6560 \text{ \AA}$ to $\sim 6760 \text{ \AA}$.